

# Symmetry-protected electronic metastability in an optically driven cuprate ladder

---

In the format provided by the authors and unedited

---

## Table of contents

1. trTDTS measurements
2. trXRD measurements
3. trXAS measurements at Cu *L*-edge
4. trXAS measurements at O *K*-edge
5. trRIXS measurements
6. DMRG calculations
7. Light-induced symmetry breaking and hopping

# 1. trTDTS measurements

## Equilibrium optical properties

In Fig. S1a, we present the temperature-dependent broadband reflectivity of  $\text{Sr}_{14}\text{Cu}_{24}\text{O}_{41}$ , previously reported in [1]. Using Kramers-Kronig relations, we obtained the real ( $\sigma_1$ ) and imaginary ( $\sigma_2$ ) parts of the optical conductivity, shown in Fig. S1b and c, respectively. The spectra indicate an insulating state at 100 K, which becomes progressively more conducting with increasing temperature, as evidenced by the enhanced low-frequency spectral weight in  $\sigma_1$ . These observations indicate a gapped charge-ordered ground state with an onset below  $T_{\text{CO}} = 250$  K, consistent with previous reports [1–3].

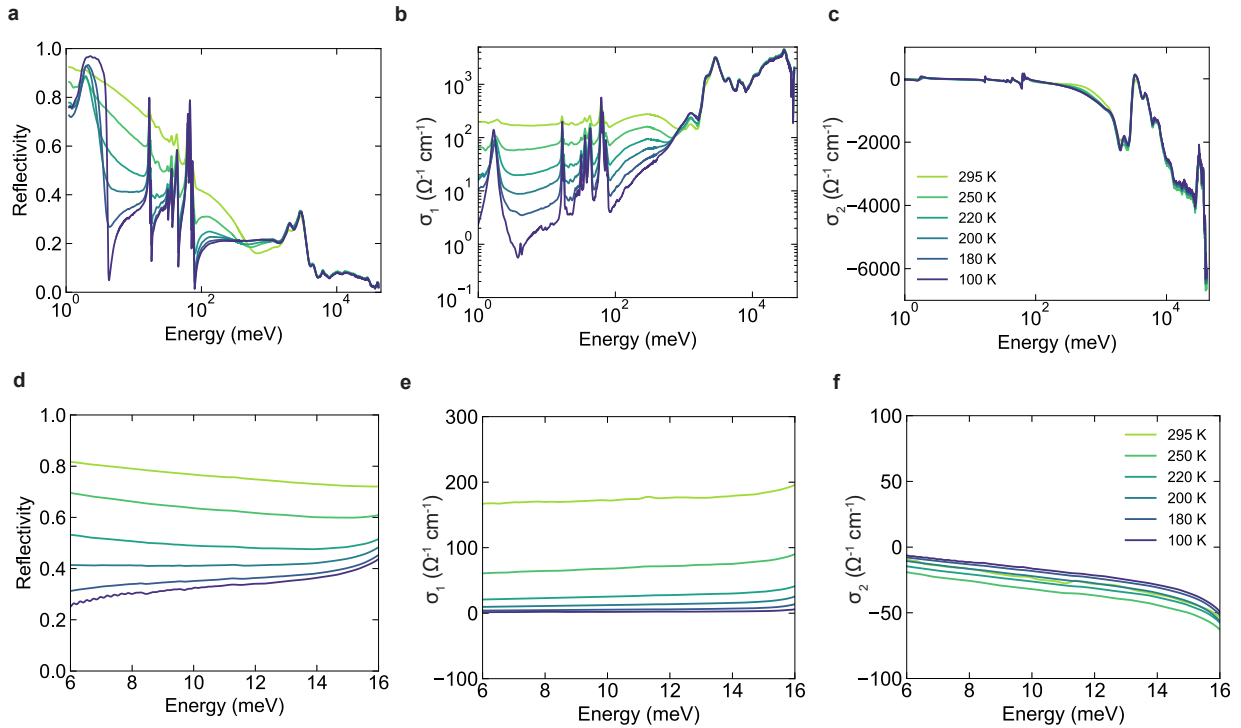


**Fig. S1. Equilibrium optical properties.** **a**, Broadband equilibrium reflectivity, and **b**, real ( $\sigma_1$ ) and **c**, imaginary ( $\sigma_2$ ) parts of the optical conductivity, as a function of temperature. **d**, Broadband equilibrium reflectivity, and **e**, real ( $\sigma_1$ ) and **f**, imaginary ( $\sigma_2$ ) parts of the optical conductivity, as a function of temperature, within the frequency range of our time-resolved time-domain THz spectroscopy measurements.

By closely examining  $\sigma_1$ , we note that the charge order gap remains unchanged with temperature. This behavior is in contrast to  $\sigma_1$  in the light-induced metastable phase (see Fig. 2d of the main text), which exhibits a suppressed charge order gap of the order of 10 meV. Notably, the charge order gap exhibits a similar suppression when  $\text{Sr}_{14}\text{Cu}_{24}\text{O}_{41}$  is substituted with Ca, as reported in [2] and reproduced in Fig. S2. The metastable state in our measurements exhibits a gap that is intermediate between that of the  $x = 3$  and  $x = 9$  compounds.

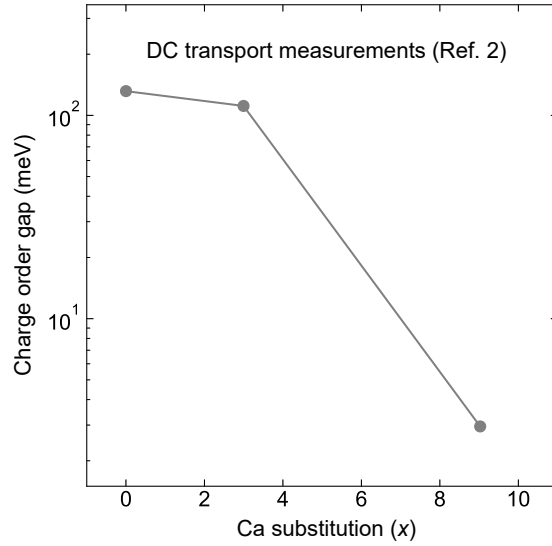


**Fig. S2. Charge order gap as a function of Ca substitution.** The charge order gap extracted from DC transport measurements, as a function of Ca substitution  $x$  in  $\text{Sr}_{14-x}\text{Ca}_x\text{Cu}_{24}\text{O}_{41}$ , reproduced from [2].

## trTDTS: Fit functions and parameters

We model the transient reflectivity in Fig. 2b of the main text by an exponential decay, with a functional form given by

$$R(t) = R_0 + \frac{1}{2} \left[ 1 + \operatorname{erf} \left( \frac{t - t_0}{\tau_0} \right) \right] A e^{-\left( \frac{t - t_0}{\tau_1} \right)}, \quad (1)$$

where  $R_0$  is the reflectivity at equilibrium,  $t_0$  is an arbitrary temporal offset, and  $\tau_1$  is an exponential decay time constant. The error function term describes the initial enhancement of reflectivity upon pump excitation, characterized by a time constant  $\tau_0$ . The fit parameters are shown in Table 1.

**Table 1.** Fit parameters in Fig. 1c.

	$R_0$	$t_0$ (ps)	$\tau_0$ (ps)	$\tau_1$ (ns)	$A$
$\omega = 15$ meV	0.372(4)	0.01(2)	0.57(5)	2.6(5)	0.383(4)

## 2. trXRD measurements

### Fit functions and parameters

The data in Fig. 3b of the main text are obtained by fitting and subtracting a fluorescent background. We detail this procedure here. In Fig. S3, we show the equilibrium and transient reciprocal space scans of the charge order diffraction peak in our time-resolved x-ray diffraction (trXRD) measurements. The charge order peak occurs over a large fluorescent background. We model these data by the sum of a linear function and a Gaussian, which describe the fluorescent background and charge order diffraction peak, respectively. The functional form is

$$I(L) = G(L; A, L_0, \sigma) + aL + b. \quad (2)$$

Here,  $I$  is the intensity, and  $L$  is the momentum transfer along  $c$ .  $G(L; A, L_0, \sigma)$  is a Gaussian function

$$G(L; A, L_0, \sigma) = \frac{A}{\sigma\sqrt{2\pi}} e^{-\frac{(L-L_0)^2}{2\sigma^2}}, \quad (3)$$

where  $A$  is the amplitude,  $L_0$  is the center, and  $\sigma$  is the width. The fit parameters are shown in Table 2. We subtract the fluorescent background shown in Fig. S3a-b to obtain the background-subtracted data in Fig. S3c and Fig. 3b of the main text.

**Table 2.** Fit parameters in Fig. 3b and Fig. S3.

	$A$ (a. u.)	$L_0$ (r. l. u.)	$\sigma$ (r. l. u.)	$a$ ( $c_L$ )	$b$ (a. u.)
Equilibrium	5.3(2)	0.2018(4)	0.0118(4)	-0.136(8)	0.056(1)
Transient	2.8(1)	0.2017(4)	0.0103(5)	-0.133(6)	0.056(1)

As described in the main text, the charge order peak center ( $L_0$ ) and width ( $\sigma$ ) remain unchanged. To show that this is representative of the charge order peak at all time delays within the metastable phase, we measured time traces at different momenta. We overlay the equilibrium and transient peaks, normalized to their peak intensities, in Fig. S4a. There is no resolvable change in the charge order peak center or width, consistent with our fit parameters in Table 2. Next, we plot the time traces of the transient charge order

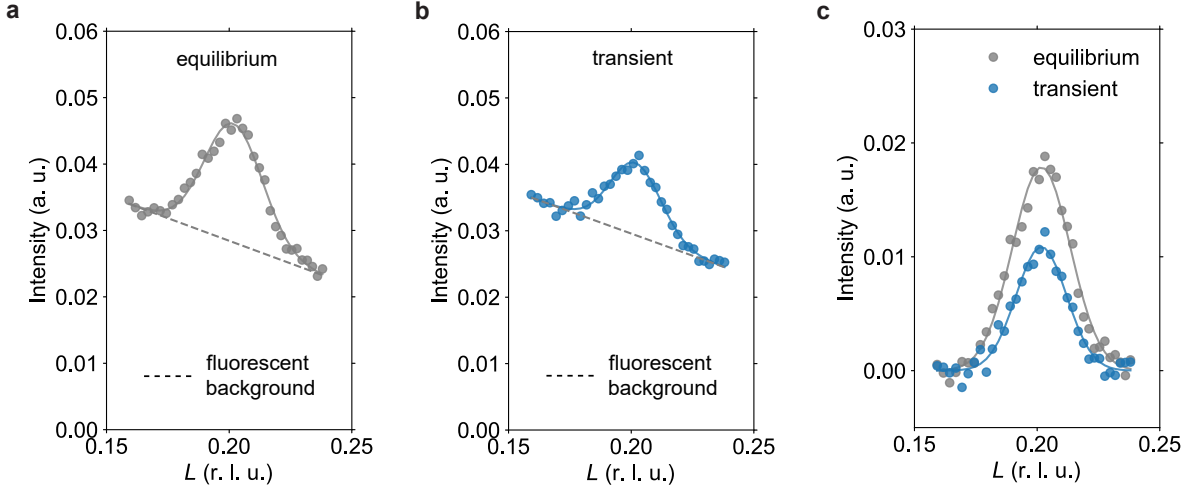


**Fig. S3. Background subtraction in trXRD data.** **a-b**, Equilibrium (a) and transient (b) time-resolved x-ray diffraction at the charge order peak, measured resonant with the O  $K$ -edge. The fluorescent background is denoted by dashed grey lines. **c**, Diffraction data from panels a and b with the fluorescent background subtracted. Solid lines denote fits.

intensity at two different momenta, namely at  $L = 0.200$  and  $0.216$ . The intensities at both momenta exhibit a step-like suppression.

We model the time delay traces by an error function given by

$$I(t) = I_0 - \frac{1}{2}A \left[ 1 + \operatorname{erf} \left( \frac{t - t_0}{\tau_0} \right) \right], \quad (4)$$

where  $\tau_0$  describes the timescale of pump-induced charge order suppression convolved with the pump-probe autocorrelation,  $I_0$  is the magnitude of the initial charge order intensity,  $A$  is the magnitude of charge order suppression, and  $t_0$  is an arbitrary temporal offset. The fit parameters are shown in Table 3. The absence of subsequent dynamics in the metastable phase shows that the charge order peak profile remains unchanged after the initial suppression.

**Table 3.** Fit parameters in Fig. S4

	$I_0$	$A$ (norm.)	$t_0$ (ps)	$\tau_0$ (ps)
$L = 0.200$	1.00(1)	0.40(1)	0.11(2)	0.21(3)
$L = 0.216$	0.46(1)	0.14(1)	0.01(2)	0.10(3)

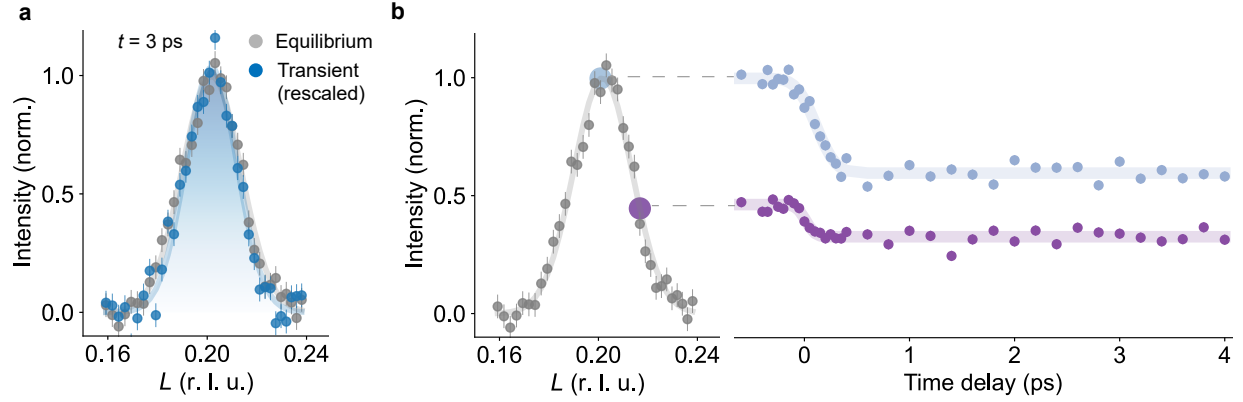


**Fig. S4. Temporal evolution of the charge order peak.** **a**, Momentum dependence of the charge order peak measured by trXRD at equilibrium and at a time delay of 3 ps, normalized, rescaled, and overlaid on each other. **b**, The charge order intensity as a function of time delay, at two fixed momenta, namely  $L = 0.200$  (light blue) and  $0.216$  (purple). The data are presented as mean values, and the error bars are given by the standard deviation of 35 datapoints measured at 255 K, where the CDW peak vanishes.

We fit the delay traces in Fig. 3c of the main text by the same function as above. We evaluate the time constant  $\tau_0$  of charge order suppression to be  $0.19(3)$  ps. The fit parameters are listed in Table 4.

**Table 4.** Fit parameters in Fig. 3c.

	$I_0$	$A$ (norm.)	$t_0$ (ps)	$\tau_0$ (ps)
$E_{\text{pump}} \parallel a$	1.00(1)	0.421(7)	0.01(4)	0.19(3)

## Fluence dependence of light-induced charge order suppression

We measure the charge order response as a function of pump fluence, with  $E_{\text{pump}} \parallel a$ , as shown in Fig. S5.

We find that the light-induced charge order suppression exhibits no recovery up to nanosecond timescales, independent of the incident fluence.

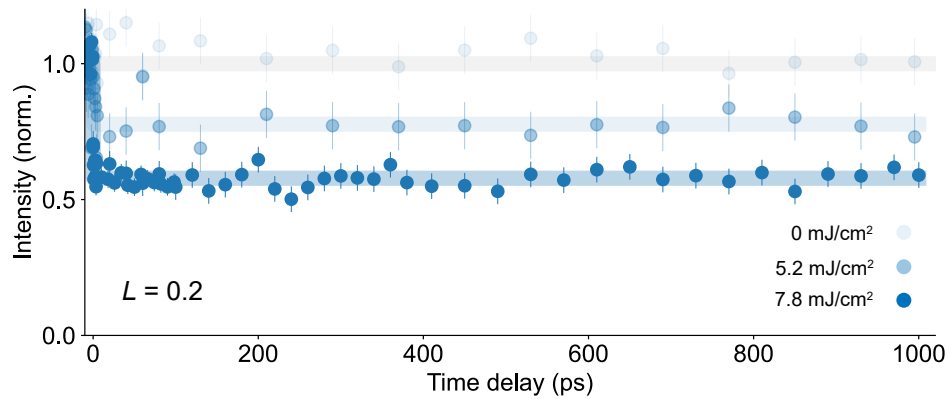


**Fig. S5. Fluence dependence of charge order suppression.** The light-induced charge order suppression is metastable up to nanosecond timescales, independent of the incident fluence. The data are presented as mean values, and the error bars are given by the standard deviation of 11 datapoints measured at negative time delays. Solid lines denote fits.

We fix  $\tau_0$  to the same value as in Table 3 and fit the data in Fig. S5. The fit results are shown in Table 5.

**Table 5.** Fit parameters in Fig. S4.

	$A$ (norm.)	$t_0$ (ps)	$\tau_0$ (ps)
5.2 mJ/cm <sup>2</sup>	0.22(1)	0.1(2)	0.19 (fixed)
7.8 mJ/cm <sup>2</sup>	0.421(7)	0.01(4)	0.19 (fixed)

### 3. trXAS measurements at Cu $L$ -edge

#### Equilibrium XAS as a function of Ca substitution

The primary effect of Ca substitution in  $\text{Sr}_{14-x}\text{Ca}_x\text{Cu}_{24}\text{O}_{41}$  is the transfer of holes from chain to ladder subunits. This hole transfer presents a characteristic signature in the Cu  $L$ -edge x-ray absorption spectra (XAS), as shown in Fig. 4d of the main text. Here, we provide a detailed account of the Cu  $L$ -edge XAS as a function of Ca substitution at equilibrium. In Fig. S6, we reproduce the XAS measured on the  $x = 0$  and  $x = 11.5$  compounds, previously reported in [4]. The two spectral features in Fig. S6 can be distinguished based on the local bonding environment, as outlined in the main text. The peak centered at 932.7 eV consists of contributions primarily from the corner-shared ladder, while the peak centered at 934.4 eV is from the edge-shared chain [5]. We model the two-peaked spectra by the sum of two Lorentzians and a linear function as

$$I(\omega) = L(\omega; A_1, \omega_{01}, \sigma_1) + L(\omega; A_2, \omega_{02}, \sigma_2) + a\omega + b, \quad (5)$$

where the Lorentzians  $L(\omega; A_i, \omega_{0i}, \sigma_i)$  describe ladder ( $i = 1$ ) and chain ( $i = 2$ ) peaks. The Lorentzian function is given by

$$L(\omega; A, \omega_0, \sigma) = \frac{A}{\pi} \left[ \frac{\sigma}{(\omega - \omega_0)^2 + \sigma^2} \right], \quad (6)$$

where  $A$ ,  $\omega_0$ , and  $\sigma$  are the amplitude, center energy, and linewidth parameters. The fit parameters are shown in Table 6.

**Table 6.** Fit parameters in Fig. S6 and Fig. 4d.

	$A_1$ (norm.)	$\omega_{01}$ (eV)	$\sigma_1$ (eV)	$A_2$ (norm.)	$\omega_{02}$ (eV)	$\sigma_2$ (eV)
$x = 0$	2.34(4)	932.650(5)	0.81(1)	1.19(3)	934.398(8)	0.69(2)
$x = 11.5$	2.70(4)	932.650(5)	0.90(1)	0.88(3)	934.42(1)	0.65(2)

We observe a reshaping of the XAS spectrum due to chain-to-ladder hole transfer in the form of a suppression of the amplitude  $A_2$  of the chain peak and an enhancement of the amplitude  $A_1$  of the ladder peak as a function of Ca substitution  $x$ .

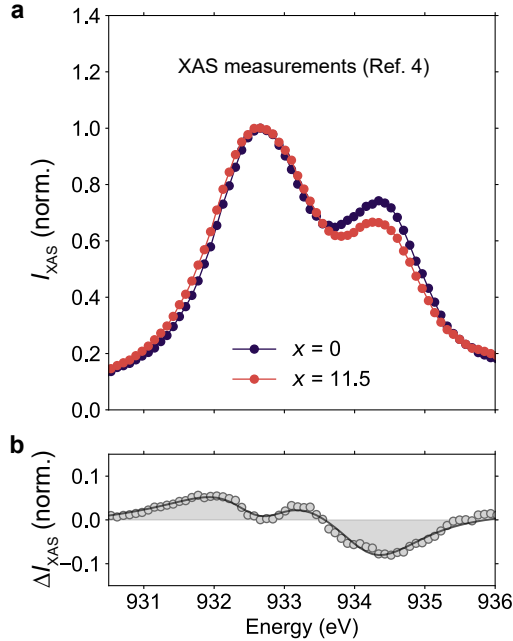


**Fig. S6. Cu  $L$ -edge XAS as a function of Ca substitution.** The static Cu  $L$ -edge x-ray absorption spectra (XAS) as a function of Ca substitution  $x$  in  $\text{Sr}_{14-x}\text{Ca}_x\text{Cu}_{24}\text{O}_{41}$ , extracted from [4]. The top panel shows the raw spectra and the bottom panel shows the difference between the  $x = 0$  and  $x = 11.5$  spectra. Solid lines are fits, as described in the text.

We further show that the spectral reshaping is linear with respect to the Ca substitution  $x$ . In Fig. S7, we plot the XAS spectra as a function of  $x$ , previously reported in [5], focusing on the well-defined suppression in the high-energy peak associated with the chain. We observe that the suppression is monotonic and linear in  $x$ , as shown in Fig. S7c. Given that the magnitude of chain-to-ladder hole transfer varies linearly with  $x$  [4–7], the magnitude of the spectral reshaping is linear with respect to  $p$ .

Finally, we confirm our interpretation of the spectral reshaping using density functional theory (DFT) calculations. We calculated the Cu  $L$ -edge XAS spectrum for isolated ladder and chain subunits, as outlined in the Methods. We first examine the spectra corresponding to the equilibrium state, where the ladder hole density is  $p = 0.06/\text{Cu}_L$ . The ladder XAS spectrum shown in Fig. S8a features a sharp peak and a continuum at higher energies. The chain XAS spectrum in Fig. S8b is somewhat broader and much weaker than the ladder one. Next, we examine the calculated spectra corresponding to the light-induced metastable state,

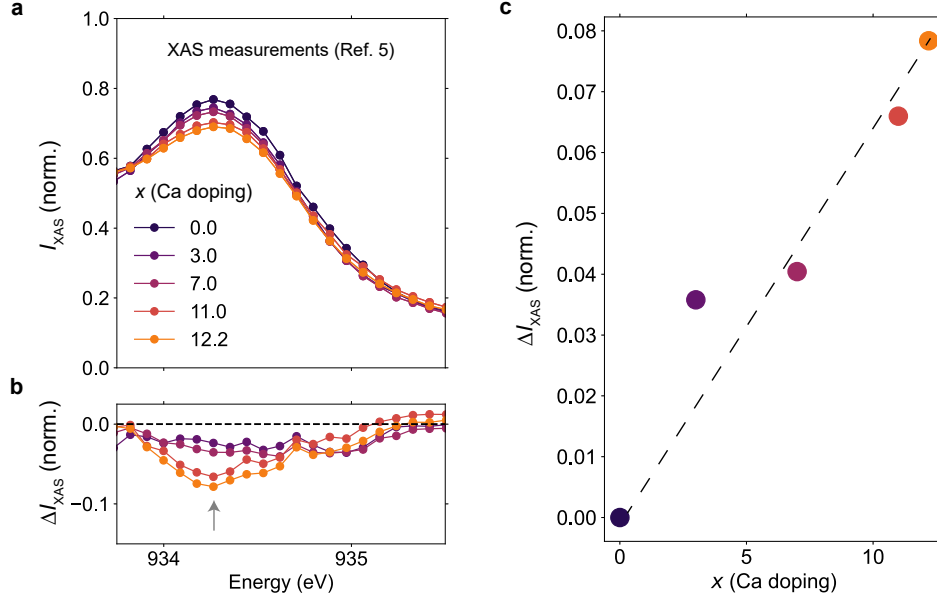


**Fig. S7. Linearity of XAS response to Ca substitution.** **a**, The static Cu  $L$ -edge x-ray absorption spectra (XAS) as a function of Ca substitution  $x$  in Sr<sub>14-x</sub>Ca<sub>x</sub>Cu<sub>24</sub>O<sub>41</sub>, extracted from [5]. **b**, The difference spectra with respect to the  $x = 0$  spectrum in panel (a). **c**, The difference intensity at 934.4 eV, denoted by the arrow in panel (b), is plotted as a function of Ca substitution  $x$ . The dashed line is a guide to the eye.

with ladder hole density  $p = 0.09/\text{Cu}_L$ . The sharp peak in the ladder XAS signal exhibits an increase in intensity and a small red shift, whereas the intensity of the chain XAS peak is strongly suppressed. These spectral changes are consistent with the addition of Cu  $3d$  holes on the ladder and the reduction of Cu  $3d$  holes on the chain. These results are in agreement with our assignment of the experimental peaks and their reshaping upon chain-to-ladder hole transfer. Finally, we note that since our calculation consists of isolated chains and ladders with different total charges (and the ensuing background charge compensation), the relative energy offset between the chain and ladder spectra cannot be determined theoretically. To overcome this limitation, we estimate the appropriate energy offset from the available experimental data (Fig. S6). Our XAS data and previous XAS measurements at the Cu  $L$  edge in the presence of Ca dopant ions define the energy positions of the ladder and chain peaks, respectively, with an energy separation of 1.6 eV. We apply the same offset to our simulated equilibrium and pumped spectra. Summing the ladder and chain spectra (Fig. S8c), we find that the calculated XAS are consistent with the experimental XAS at equilibrium,

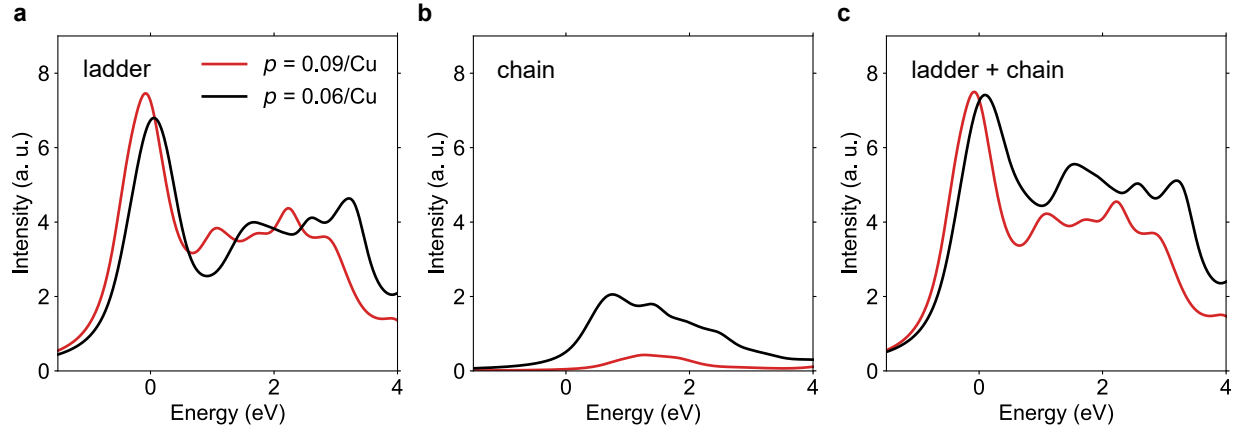


**Fig. S8. Spectral decomposition of Cu L edge XAS calculated by DFT.** Density functional theory (DFT) calculation of the Cu *L*-edge x-ray absorption spectra (XAS) of **a**, the ladder subunit and **b**, the chain subunit, for ladder hole densities  $\rho = 0.06/\text{Cu}_L$  and  $0.09/\text{Cu}_L$ . **c**, The sum of the spectra in panels (a) and (b).

reproducing both the suppression of the high-energy peak associated with the chains and the enhancement of the low-energy shoulder of the peak associated with the ladders.

## trXAS measurements

We model the trXAS spectra in Fig. 3a-b of the main text using the same functional form as in Eq. 5 and 6. The fit parameters are shown in Table 7.

**Table 7.** Fit parameters in Fig. 3a-b

	$A_1$ (norm.)	$\omega_{01}$ (eV)	$\sigma_1$ (eV)	$A_2$ (norm.)	$\omega_{02}$ (eV)	$\sigma_2$ (eV)
Equilibrium	1.88(3)	932.611(5)	0.73(1)	1.18(3)	934.333(8)	0.74(2)
Transient	1.95(3)	932.600(5)	0.75(1)	1.26(4)	934.32(1)	0.83(2)

Next, we present the temporal evolution of the trXAS results described in Fig. 4 of the main text. The delay traces at energies fixed to 932.0 eV and 934.4 eV, corresponding to the ladder and chain peaks, respectively, are presented in Fig. S9a. The data show that the light-induced reshaping of the trXAS spectra has a short-lived initial response, followed by a long-lived metastable response. We model the time dependence using the following functional form:

$$I(t) = \frac{1}{2} \left[ 1 + \operatorname{erf} \left( \frac{t - t_0}{\tau_0} \right) \right] \left[ B_0 + B_1 e^{-\frac{(t-t_0)}{\tau_1}} \right], \quad (7)$$

where  $\tau_0$  describes the timescale of the pump-induced response convolved with the pump-probe auto-correlation,  $B_0$  is the magnitude of the metastable response,  $B_1$  and  $\tau_1$  are the amplitude and decay time constant of the short-lived response, respectively, and  $t_0$  is an arbitrary temporal offset. Fitting the delay traces in Fig. S9a, we obtain the fit parameters listed in Table 8.

**Table 8.** Fit parameters in Fig. S8a

	$t_0$ (ps)	$\tau_0$ (ps)	$B_0$ (norm.)	$B_1$ (norm.)	$\tau_1$ (ps)
Ladder	0.02(2)	0.13(3)	0.123(6)	0.267(4)	0.33(8)
Chain	0.1(1)	0.2(1)	0.125(2)	0.10(3)	0.50(1)

The primary light-induced effect is the transient activation of the apical hopping pathway and the resulting metastable chain-to-ladder hole transfer, which we observe as the long-lived response in our trXAS delay traces. We additionally observe a short-lived signal at both the ladder and chain resonances. Since the pump

photon energy (1.55 eV) is close to the charge transfer gap of the ladder (2 eV) [6], we posit that a fraction of the pump photons additionally generates holon-doublon pairs, giving rise to the observed short-lived signal. The amplitude of this signal is smaller at the chain resonance, consistent with the larger chain charge transfer gap (3 eV) [6]. Interestingly, we do not observe a prominent short-lived signal in the trTDTS (Fig. 2) and trXRD (Fig. 3) delay traces, suggesting that the charge order does not exhibit a comparable short-lived response. This discrepancy in the fast dynamics remains an open question.

Finally, we present the field dependence of the light-induced reshaping of the trXAS spectra. In Fig. S9b, we plot the normalized response in the metastable state ( $t = 3$  ps) as a function of the square of the pump field, with the energies fixed at 932.0 eV (ladder) and 934.4 eV (chain). The response scales linearly with the square of the pump field, as indicated by the dashed line, consistent with the light-induced symmetry-breaking mechanism outlined in the main text and SI Section 7.

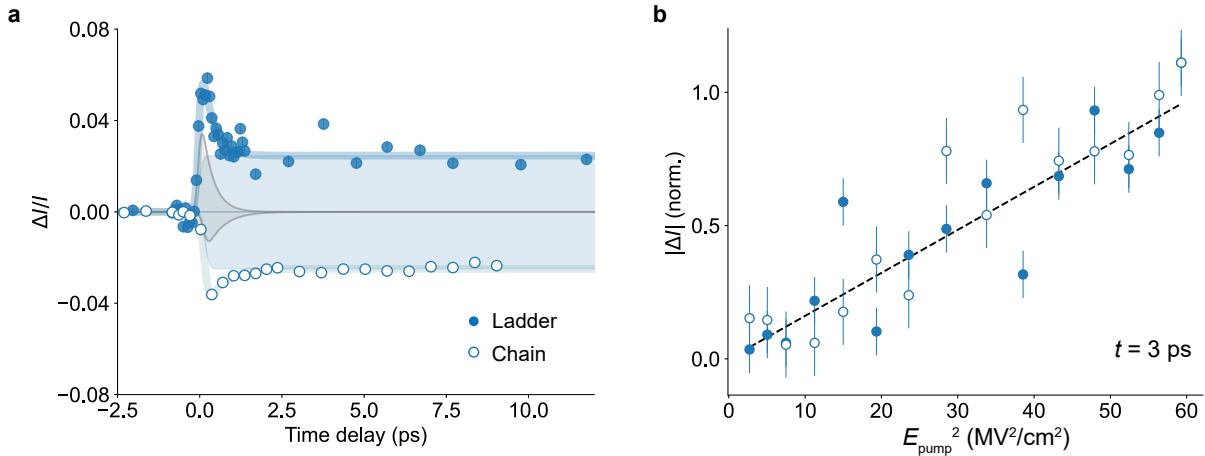


**Fig. S9. Temporal evolution and pump field dependence of trXAS spectra.** **a**, Traces of the temporal evolution at fixed energies, 932.0 eV (labeled ‘Ladder’) and 934.4 eV (labeled ‘Chain’). Fits are denoted by solid lines. The short-lived and long-lived components are shaded in grey and blue, respectively. **b**, The normalized response as a function of the pump field at a time delay of 3 ps. The data are presented as mean values, and the error bars are given by the standard deviation of 10 datapoints measured at negative time delays. The dashed line is a guide to the eye.

## 4. trXAS measurements at O $K$ -edge

We first examine the equilibrium O  $K$ -edge x-ray absorption spectra (XAS) as a function of Ca substitution for  $x = 0$  and  $x = 11.5$  (see Fig. S10), which we reproduce here from Ref. [4]. The spectra consist of two primary features: a peak centered at 528.2 eV, corresponding to the doped holes, also referred to as the Zhang-Rice singlet (ZRS) peak, and a peak centered at 529.5 eV, corresponding to the upper Hubbard band (UHB). In cuprates, an increase in the overall hole density is generally associated with a suppression of the UHB and an enhancement of the ZRS [8]. While chain and ladder contributions to the O  $K$ -edge XAS cannot be unambiguously distinguished (unlike what is observed at the Cu  $L$ -edge) due to overlapping spectral features, previous studies have established clear qualitative trends associated with chain-to-ladder hole transfer [4], which we summarize below.

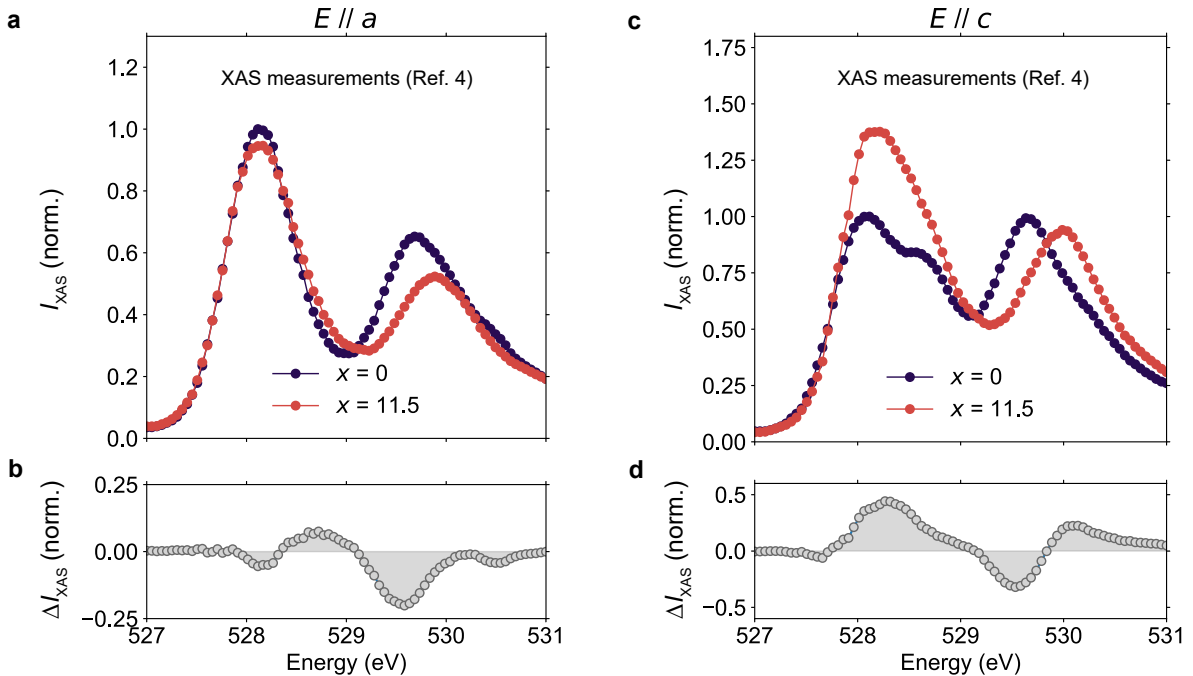


**Fig. S10. O  $K$ -edge XAS as a function of Ca substitution.** **a**, The static O  $K$ -edge x-ray absorption spectra (XAS) as a function of Ca substitution  $x$  in  $\text{Sr}_{14-x}\text{Ca}_x\text{Cu}_{24}\text{O}_{41}$  for x-rays polarized along  $a$ , extracted from [4]. **b**, The difference between the  $x = 0$  and  $x = 11.5$  spectra shown in panel a. **c-d**, Same as panels a-b, for x-rays polarized parallel to  $c$ . Lines are a guide to the eye.

With x-rays polarized parallel to  $a$ , the ZRS and UHB are both suppressed with increasing chain-to-ladder hole transfer. With x-rays polarized parallel to  $c$ , the ZRS features an additional peak centered at 528.7 eV that is attributed to holes in the ladder subunit. Hence, chain-to-ladder hole transfer in this case causes an enhancement of the ZRS together with a suppression of the UHB.

Finally, we note that the UHB exhibits a significant blue shift with increasing Ca substitution, for both x-ray polarizations. The UHB of the ladder and chain subunits overlap in energy [4]. If hole transfer were to shift the UHB, the ladder and chain contributions would shift in opposite directions since holes are added to the former and subtracted from the latter. This would manifest as a broadening of the UHB with Ca substitution  $x$ , rather than a blue shift. The blue shift is more naturally explained in terms of the structural changes that occur when 82% of the Sr atoms are replaced by Ca. The most dominant of these is along the  $b$  direction. Ca substitution ( $x = 12$ ) causes a decrease of the overall lattice parameter  $b$  by 7% [Ammerahl], and increases distortions of the ladder O atoms along  $b$  by a factor of 10 [9]. The latter in particular would modify the local bonding environment and hence influence the O  $K$ -edge XAS peak positions.

Hence, we expect that light-driven chain-to-ladder hole transfer, which occurs without the structural distortions associated with Ca substitution, will manifest in the form of the spectral reshaping described above but without the additional blue shift of the UHB.

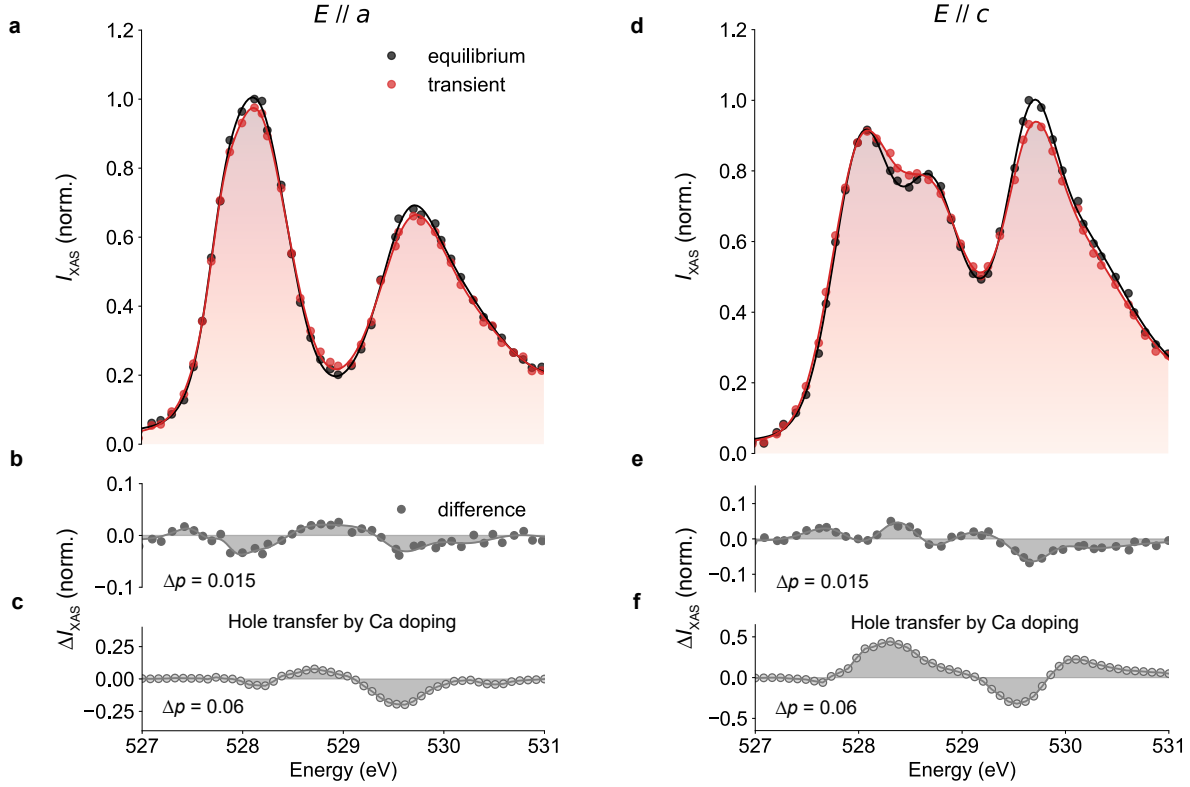


**Fig. S11. O  $K$ -edge trXAS.** **a**, Equilibrium (black) and transient (red) O  $K$ -edge x-ray absorption spectra (XAS) at pump-probe delay  $t = 3$  ps, for x-rays polarized along  $a$ . **b**, Difference between equilibrium and transient XAS intensities. **c**, Change in static XAS intensity due to chain-to-ladder hole transfer induced by Ca substitution in  $\text{Sr}_{14-x}\text{Ca}_x\text{Cu}_{24}\text{O}_{41}$ , derived from reference [4]. The data show the difference between XAS measured on the  $x = 0$  and  $x = 11.5$  compounds, which corresponds to a charge transfer of  $\Delta p = 0.06$  holes/ $\text{Cu}_L$ . **d-f** Same as panels a-c, for x-rays polarized parallel to  $c$ .

We show the results of our O  $K$ -edge trXAS measurements (pump polarization parallel to  $c$  in all measurements) in Fig. S11. Note that the pump fluence of  $3.9 \text{ mJ/cm}^2$  used in these measurements is half that used for the Cu  $L$ -edge trXAS measurements. The transient spectrum with x-ray polarization  $E \parallel a$  exhibits a reshaping with both the ZRS and UHB suppressed relative to the equilibrium spectra, consistent with our expectations for chain-to-ladder hole transfer. The difference spectrum in S11b is in excellent agreement with the difference spectrum due to Ca substitution in Fig. S11c, rescaled by a factor of 4. This corresponds to a hole transfer of  $0.06/4 = 0.015$  holes/ $\text{Cu}_L$ . For x-ray polarization  $E \parallel c$ , shown in Fig. S11d,

we observe a suppression of the UHB and an enhancement of the ZRS, consistent with a chain-to-ladder hole transfer without the structural distortions associated with Ca substitution. The lack of signatures of structural distortions in the light-induced hole transfer implies that light-induced doping is distinct from that due to Ca substitution at equilibrium.

We plot the temporal evolution of the O  $K$ -edge trXAS spectra in Fig. S12. While both polarizations and resonances exhibit the metastable component due to chain-to-ladder hole transfer, the short-lived signal assigned to holon-doublons is only prominent in the  $E \parallel a$  spectrum at the ZRS.

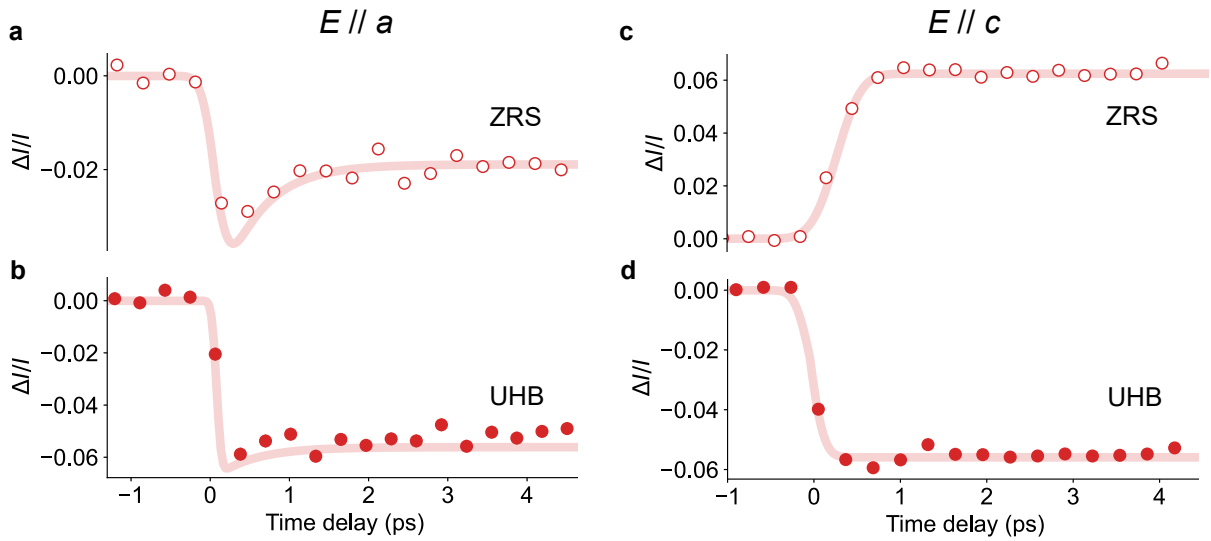


**Fig. S12. Temporal evolution of O  $K$ -edge trXAS spectra.** **a-b**, Traces of the temporal evolution at fixed energies, 528.0 eV (labeled ‘ZRS’) and 529.7 eV (labeled ‘UHB’), for x-rays polarized parallel to  $a$ . **c-d**, Traces of the temporal evolution at fixed energies, 528.4 eV (labeled ‘ZRS’) and 529.7 eV (labeled ‘UHB’), for x-rays polarized parallel to  $c$ .

In summary, our O  $K$ -edge trXAS measurements corroborate the chain-to-ladder hole transfer detected and quantified by our Cu  $L$ -edge trXAS measurements described in the main text.

## 5. trRIXS measurements

### Triplon excitations

The ladder subunit of  $\text{Sr}_{14}\text{Cu}_{24}\text{O}_{41}$  is composed of spin singlets. The fundamental magnetic excitations of this system are dispersive singlet-to-triplet excitations known as ‘triplons,’ shown schematically in Fig. S13. The symmetry of the ladder geometry implies that sectors of even and odd triplon number do not mix in the RIXS spectra, due to different parity with respect to reflection about the center of the ladder legs. In particular, with  $H = 0$ , as in our measurements, we only detect excitations with an even triplon number, which are dominated by the two-triplon continuum. We note that the inclusion of doped holes in the ladder disrupts the singlet background (see Fig. S13) and reduces the overall triplon scattering intensity, as discussed in the main text.

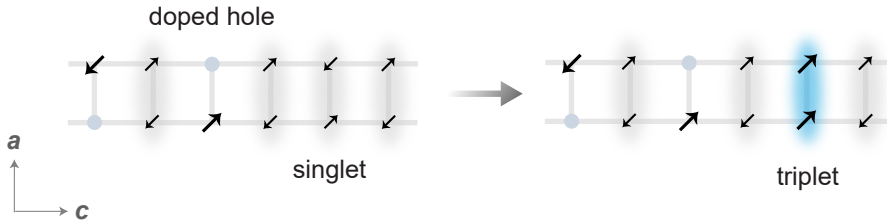


**Fig. S13. Triplon excitation** Schematic of dispersing singlet-to-triplet excitations called ‘triplons.’ The black arrows represent spins, grey circles represent doped holes, grey clouds represent spin singlets, and the blue cloud represents a spin triplet excitation.

### Subtraction of elastic peak

The Cu  $L$ -edge RIXS spectra of  $\text{Sr}_{14}\text{Cu}_{24}\text{O}_{41}$  consist of an elastic peak at zero energy loss, a phonon centered at 60 meV, triplons dispersing up to 400 meV for finite  $L$ , and  $dd$  orbital excitations above 1.3 eV. Due to the combined energy resolution of our spectrometer, the elastic and phonon peaks cannot be distinguished from each other. We also note that for  $\pi$  incident x-rays, as in our measurements, the phonon scattering intensity is much weaker than the elastic and spin-flip magnetic excitations. Given these two conditions, we assume that the convolution of the elastic and phonon peaks is approximately symmetric about zero energy loss. We

fit the low-energy shoulder of this contribution to a Gaussian peak and subtract it from our RIXS spectra to isolate the magnetic scattering intensity below 1 eV. We assume that any residual contribution from the phonon is negligible compared to the magnetic excitations, especially away from the zone center ( $L = 0$ ).

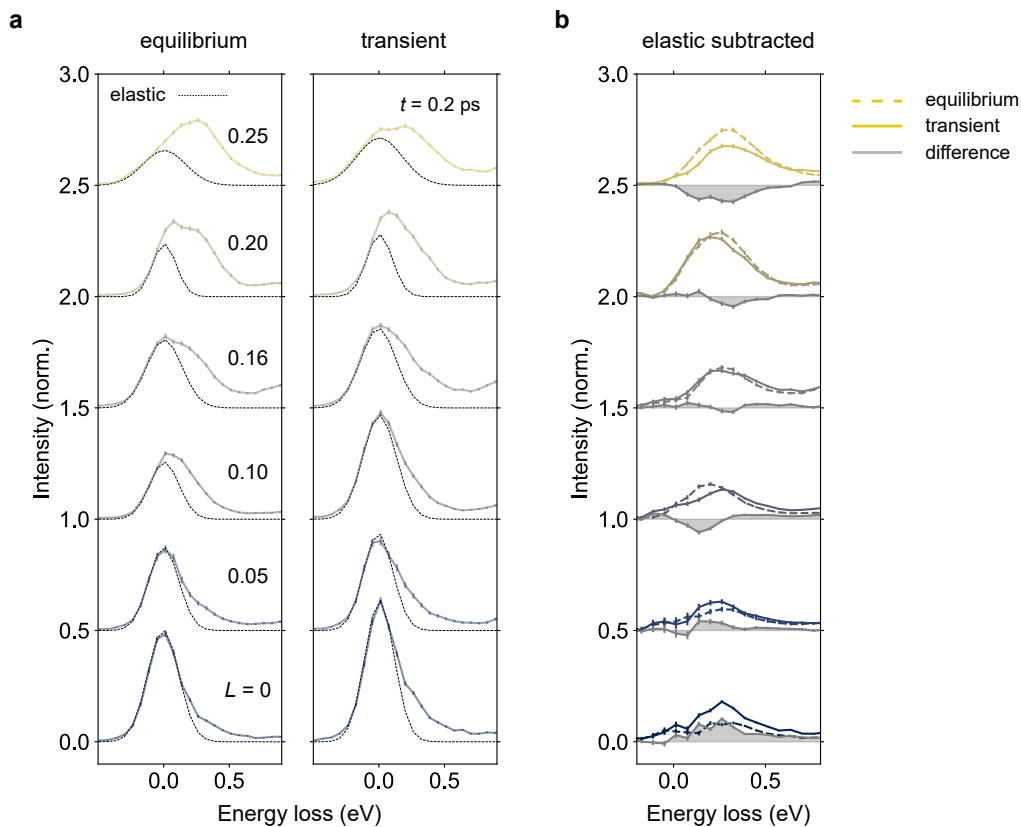


**Fig. S14. Raw trRIXS spectra at  $t = 0.2$  ps.** **a**, Equilibrium and transient time-resolved resonant inelastic x-ray scattering (trRIXS) spectra as a function of momentum  $L$ , at pump delay  $t = 0.2$  ps, normalized to the total intensity of  $dd$  excitations. The elastic component is denoted by the dashed black line. **b**, trRIXS spectra with the elastic components subtracted. The difference between equilibrium and transient spectra is shown in grey. The data are presented as mean values, and error bars are estimated as the square root of the raw intensity counts, assuming Poisson statistics.

We implement this elastic peak subtraction separately for the equilibrium and transient spectra at each measured momentum  $L$  and pump delay  $t$ . In Fig. S14, we show our results for trRIXS spectra measured as a function of  $L$  with  $t$  fixed to 0.2 ps. In Fig. S14b, we show the spectra with the elastic peak subtracted.

In Fig. S15, we show the corresponding results for the  $L$ -dependent trRIXS spectra at  $t = 3$  ps, and in Fig. S16, the corresponding results for the  $t$ -dependent trRIXS spectra at  $L = 0.25$ .

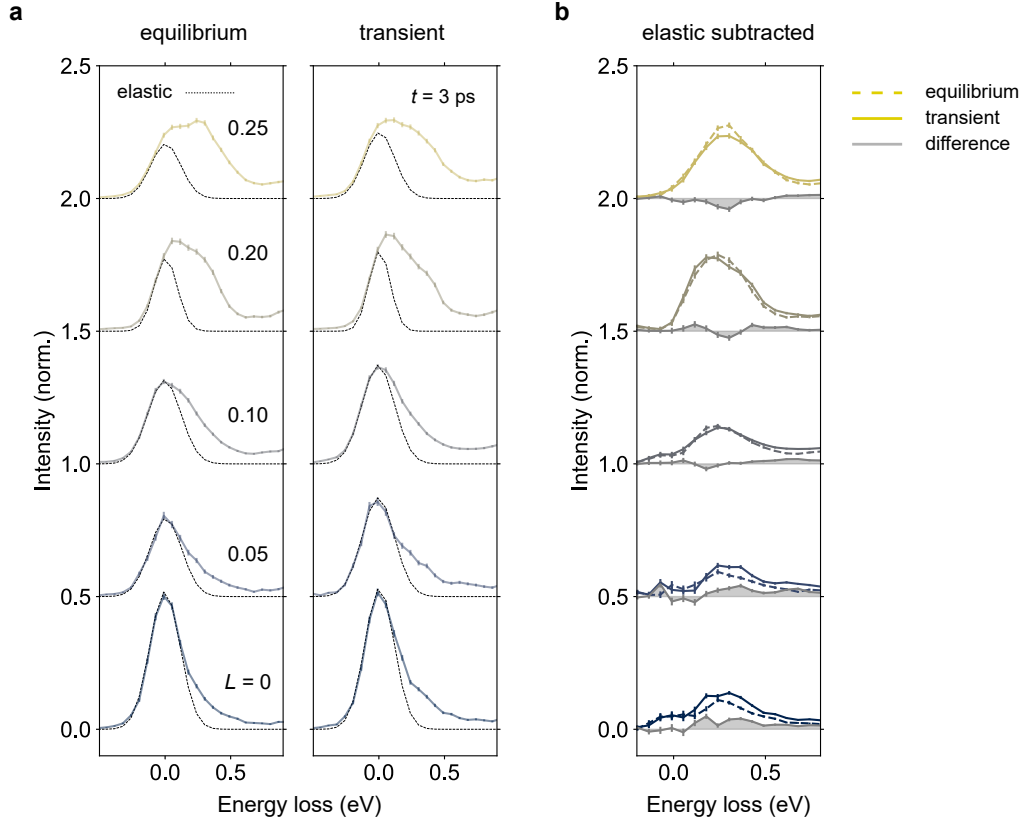


**Fig. S15. Raw trRIXS spectra at  $t = 3$  ps.** **a**, Equilibrium and transient time-resolved resonant inelastic x-ray scattering (trRIXS) spectra as a function of momentum  $L$ , at pump delay  $t = 3$  ps, normalized to the total intensity of  $dd$  excitations. The elastic component is denoted by the dashed black line. **b**, trRIXS spectra with the elastic components subtracted. The difference between equilibrium and transient spectra is shown in grey. The data are presented as mean values, and error bars are estimated as the square root of the raw intensity counts, assuming Poisson statistics.

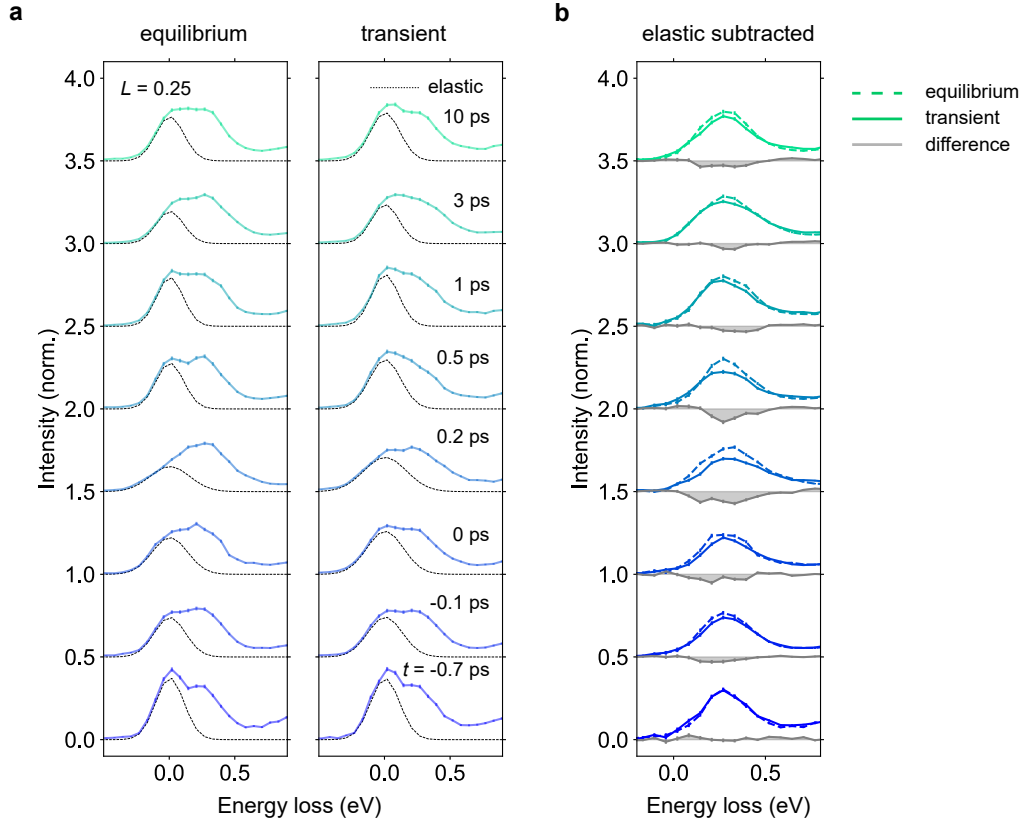


**Fig. S16. Raw trRIXS spectra at  $L = 0.25$ .** **a**, Equilibrium and transient time-resolved resonant inelastic x-ray scattering (trRIXS) spectra as a function of pump delay  $t$ , at momentum  $L = 0.25$ , normalized to the total intensity of  $dd$  excitations. The elastic component is denoted by the dashed black line. **b**, trRIXS spectra with the elastic components subtracted. The difference between equilibrium and transient spectra is shown in grey. All spectra are normalized to the total intensity of  $dd$  excitations. The data are presented as mean values, and error bars are estimated as the square root of the raw intensity counts, assuming Poisson statistics.

## Extracting $\text{tr}S(q, \omega)$ from trRIXS spectra

To extract the dynamical spin structure factor  $S(q, \omega)$  from the RIXS spectra, we first subtract the non-magnetic components of the scattered signal, as outlined in the previous section. Next, we normalize the subtracted RIXS spectra by scaling them by a geometry-dependent factor to ensure the total integrated intensity of the orbital excitations matches the theoretical single-ion scattering cross-section calculated using exact diagonalization (ED) [10]. We do this by considering orbital excitations of a  $\text{Cu}^{2+}$  ion in a square-planar crystal field, neglecting spin-flip and phonon contributions. In this section,  $x$ ,  $y$ , and  $z$  are parallel to the crystallographic  $a$ ,  $c$ , and  $b$  directions, respectively. We fix the crystal field parameters by matching the theoretical spectra to the experimental orbital excitation energies, and obtain  $D_q = 0.164$  eV,  $D_s = 0.42$  eV, and  $D_t = 0.19$  eV. In Fig. S17a-b, we show the experimental and calculated RIXS spectra as a function of momentum  $L$ . The integrated intensity of orbital excitations is plotted as a function of the incident angle  $\theta$  in Fig. S17c. We multiply the experimental spectra in Fig. S17a by a  $\theta$ -dependent factor to match this dependence within an overall scale factor. We refer to these spectra as the ‘normalized RIXS spectra.’

Finally, we extract  $S(q, \omega)$  as follows. The RIXS magnetic excitation signal is proportional to  $S(q, \omega)$  multiplied by the form factor of the single-ion spin-flip scattering cross-section,  $R_{\text{spin}}(\epsilon, \epsilon', \Omega_i)$ , where  $\Omega_i$  is the excitation energy and  $\epsilon$  and  $\epsilon'$  are the polarizations of incident and scattered photons [11, 12]

$$I_{\text{spin}} \propto R_{\text{spin}}(\epsilon, \epsilon', \Omega_i) \times S(q, \omega). \quad (8)$$

Even though this formalism does not account for hole doping, its validity for doped systems within the energy range of magnetic excitations has been verified in Ref. [13]. We calculate  $R_{\text{spin}}$  for a hole in a  $d_{x^2-y^2}$  orbital with its spin oriented in-plane along  $[1, 0, 1]$ , following the approach in previous publications [11, 14]. The results are plotted in Fig. S17d. We obtain  $S(q, \omega)$  up to an overall scaling factor by dividing the normalized RIXS spectra by  $R_{\text{spin}}$ . We apply these steps to both the equilibrium and transient RIXS spectra, subtracting them to obtain the time-resolved  $S(q, \omega)$  spectra shown in Fig. 5 of the main text.

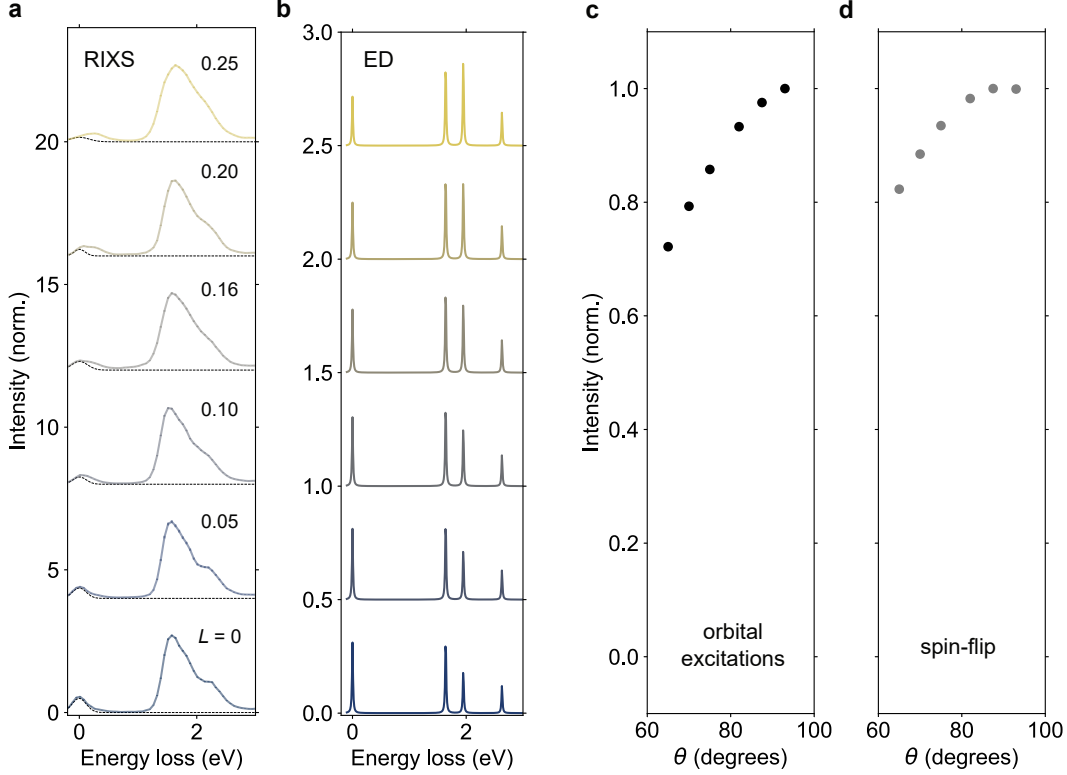


**Fig. S17. ED calculations to extract  $S(q, \omega)$  from RIXS.** **a**, Equilibrium resonant inelastic x-ray scattering (RIXS) spectra as a function of momentum  $L$ , normalized to the total intensity of  $dd$  excitations. **b**, Orbital excitation spectra calculated using exact diagonalization (ED) for  $\pi$ -polarized x-rays. **c-d**, Integrated orbital excitation scattering cross-section (c) and spin-flip cross-section (d) as a function of incident angle  $\theta$ .

### Temporal evolution of $\text{tr}S(q, \omega)$

Here, we expand upon the results presented in Fig. 5 of the main text and show the temporal evolution of the two-triplon continuum in Fig. S18. At longer timescales, the intensity reduction is fully captured by the metastable hole transfer, as confirmed by the agreement with DMRG calculations (Fig. S18b). However, at shorter timescales, the magnetic signal exhibits a much stronger suppression, which recovers on a sub-picosecond timescale. This behavior mirrors the time evolution of the trXAS spectra (Fig. S9a), tentatively assigned to short-lived photoinduced holon-doublons within the ladders, as detailed in Section 3.

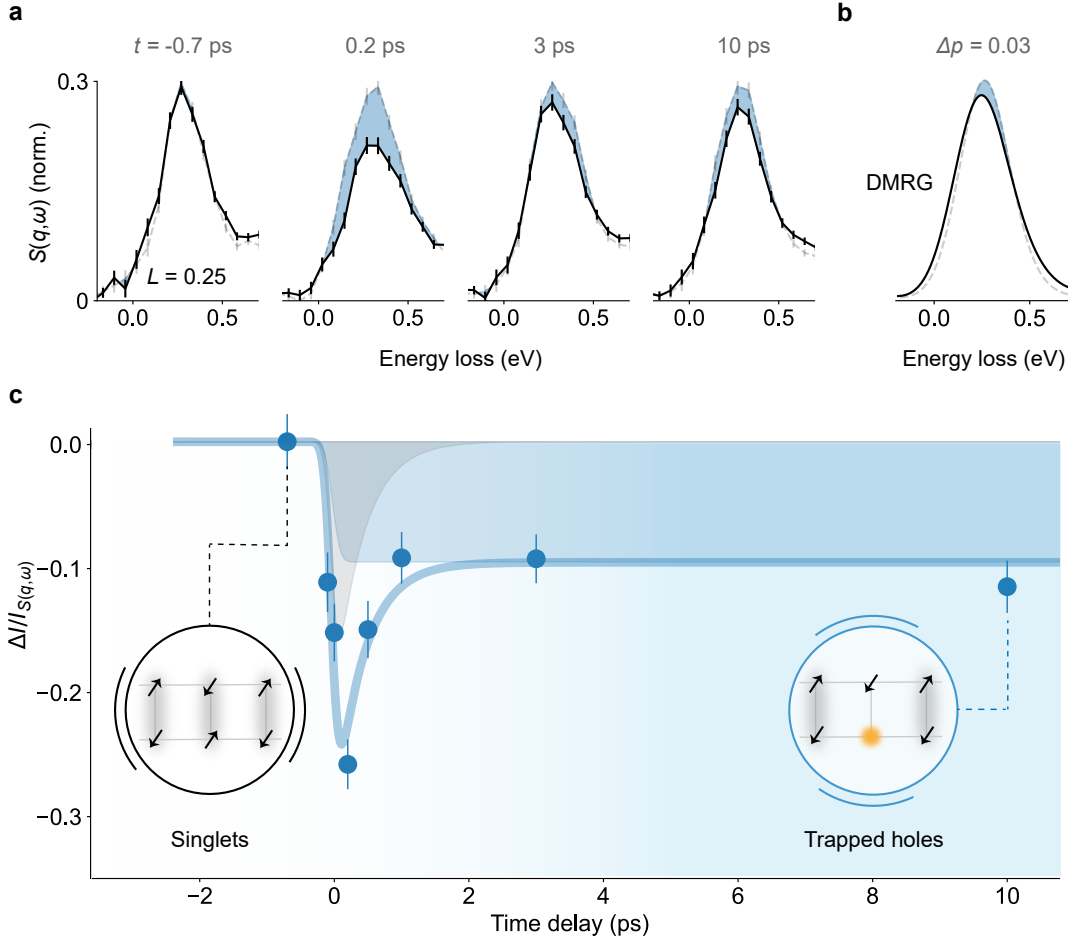


**Fig. S18. Temporal evolution of two-triplon continuum.** **a**,  $S(q, \omega, t)$  at  $q = 0.25$  in (grey) and out of equilibrium (black) for selected time delays. After an initial suppression and a partial recovery attributed to short-lived photo-induced holon-doublons, the two-triplon continuum exhibits a residual metastable intensity suppression. **b**, DMRG calculation of  $S(q, \omega)$  for  $p = 0.06$  (grey, equilibrium) and  $p = 0.09$  (black, transient). The calculated two-triplon suppression matches that observed in the trRIXS spectra at long timescales. **c**, Time-dependent differential two-triplon intensity  $\Delta I / I_{S(q, \omega)}$  as a function of time delay. The data are presented as mean values, and error bars are estimated as the square root of the raw intensity counts, assuming Poisson statistics. Sketches of the chain-to-ladder hole transfer and the consequent disruption of short-range spin correlations are shown in the bubbles. Arrows denote spins, yellow circles denote holes, and the grey clouds indicate rung singlets.

## 6. DMRG calculations

To identify spectral fingerprints of hole doping, we employ the density matrix renormalization group (DMRG) to simulate the dynamical spin structure factor  $S(q, \omega)$  in a two-leg ladder system. The system length is chosen as  $L = 64$ . Based on the quantitative experiment-theory comparisons in Ref. [15], this ladder system can be faithfully described by a single-band extended Hubbard model, with its Hamiltonian given by:

$$\begin{aligned} \mathcal{H} = & - \sum_{jl\sigma} t [c_{j\sigma}^{(l)\dagger} c_{j+1\sigma}^{(l)} + h.c.] - \sum_{j\sigma} t_{\perp} [c_{j\sigma}^{(0)\dagger} c_{j\sigma}^{(1)} + h.c.] - \sum_{jl\sigma} t' [c_{j\sigma}^{(l)\dagger} c_{j+1\sigma}^{(1-l)} + h.c.] \\ & + U \sum_{jl} n_{j\uparrow}^{(l)} n_{j\downarrow}^{(l)} + V \sum_j \sum_{\sigma, \sigma'} [n_{j\sigma}^{(0)} n_{j\sigma'}^{(1)} + \sum_l n_{j\sigma}^{(l)} n_{j+1\sigma'}^{(l)}], \end{aligned} \quad (9)$$

where  $c_{j\sigma}^{(l)}$  ( $c_{j\sigma}^{(l)\dagger}$ ) annihilates (creates) an electron at site  $j$  on leg  $l = 0, 1$  with spin  $\sigma = \uparrow, \downarrow$ , and  $n_{j\sigma}^{(l)} = c_{j\sigma}^{(l)\dagger} c_{j\sigma}^{(l)}$  denotes the local electron density. Here,  $t$  is the hopping integral between nearest neighbors along the leg,  $t_{\perp} = 0.84t$  is the hopping along the rung, and  $t' = -0.3t$  is the next-nearest neighbor hopping. The on-site Hubbard repulsion is  $U = 8t$ , and the nonlocal, likely phonon-mediated, attractive interaction is  $V = -1.25t$  [15–17]. In this particular system, we find that a maximum bond dimension  $D = 1000$  gives truncation error magnitudes on the order of  $10^{-7}$ .

The dynamical spin structure factor  $S(q, \omega)$  is

$$S(q, \omega) = \int_0^{T_{\max}} dt \sum_j \sum_{l=0,1} \langle G | \mathcal{U}(0, t) S_j^{(l)} \mathcal{U}(t, 0) S_{j_0}^{(0)} | G \rangle e^{iqj} e^{-i\omega t} e^{-t^2/t_{\text{win}}^2}. \quad (10)$$

Here,  $S_j^{(l)} = [c_{j\uparrow}^{(l)\dagger} c_{j\uparrow}^{(l)} - c_{j\downarrow}^{(l)\dagger} c_{j\downarrow}^{(l)}]/2$  is the spin operator at site  $j$  on leg  $l$ , and  $\mathcal{U}(t_1, t_2)$  is the time-evolution operator. To minimize boundary effects and enforce translational symmetry, the middle site  $j_0 = L/2$  is fixed, and the sum in Eq. (10) runs over all site indices  $j$ . The two-time correlation function is evaluated using the time-dependent variational principle (TDVP), with a step size  $\delta t = 0.05t^{-1}$  and a maximum time  $T_{\max} = 30t^{-1}$ . The finite-time Fourier transform is applied using a Gaussian window function with the parameter  $t_{\text{win}} = 300t^{-1}$ .

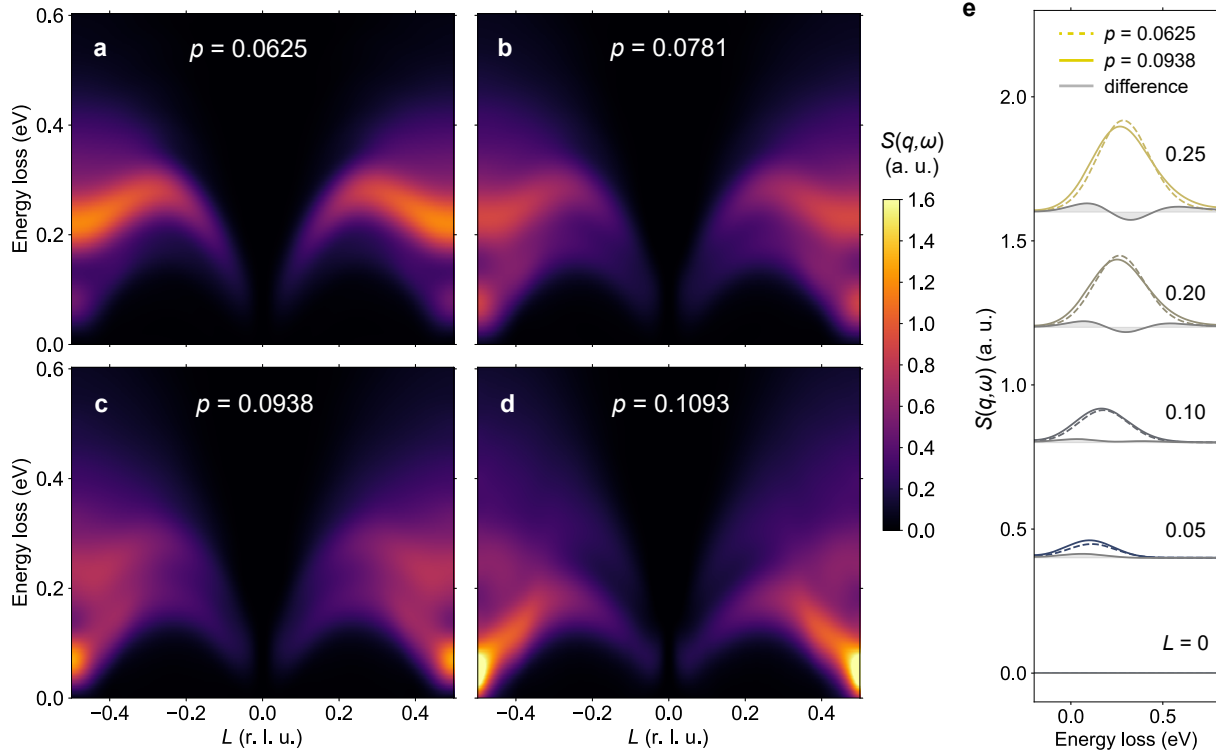


**Fig. S19.**  $S(q, \omega)$  calculated by DMRG. **a-d**,  $S(q, \omega)$  intensity maps for ladder hole densities, from  $p = 0.0625/\text{Cu}_L$  to  $p = 0.1093/\text{Cu}_L$ , calculated using DMRG. **e**,  $S(q, \omega)$  spectra as a function of momentum  $L$ , for  $p = 0.0625/\text{Cu}_L$  and  $p = 0.0938/\text{Cu}_L$ , broadened to match the experimental energy resolution of 260 meV. The difference between the two spectra is shown in grey.

To account for the self-doping at equilibrium, a hole density  $p = 0.0625/\text{Cu}_L$  is set as the reference, with additional hole doping and impurities introduced relative to this. As shown in Fig. S19a, the spectrum with hole density  $p = 0.0625/\text{Cu}_L$  is most intense for the two-triplon continuum between 0.2 and 0.4 eV. A lower excitation branch, originating from quasiparticle spin-flips, is visible between 0.05 and 0.15 eV [7, 15, 18–21].

### Variation of $S(q, \omega)$ with hole doping

To quantify the photoinduced doping in the metastable state, we examine the  $S(q, \omega)$  obtained for hole densities of  $p = 0.0781/\text{Cu}_L$ ,  $0.0938/\text{Cu}_L$ , and  $0.1093/\text{Cu}_L$  (see Fig. S19b-d). With increasing hole density, the spin spectral weight transfers from the two-triplon continuum to the quasiparticle branch.

To enable comparison with the experimental results (Fig. 5 of the main text), we convolve the simulated spectra with a Gaussian broadening, matching the experimental energy resolution of 260 meV. We present

the convolved spectra with  $p = 0.0625/\text{Cu}_L$  and  $p = 0.0938/\text{Cu}_L$  as a function of momentum in Fig. S19e. Hole doping results in a broadening and slight red shift of the two-triplon intensity at  $L > 0.10$ . This manifests as a slight suppression of the peak intensity and a slight increase at the shoulders, as shown in the difference plots (filled grey area). At larger doping, such as in  $p = 0.1093/\text{Cu}_L$ , we find a significant suppression of the two-triplon continuum and transfer of spectral weight to the quasiparticle branch, which is inconsistent with the experimental observations (see Fig. S15 and Fig. 5 of the main text). Thus we find that  $p = 0.0938/\text{Cu}_L$  offers the best agreement with the experimental  $S(q, \omega)$  in the metastable state.

### Effect of hole localization

To determine whether the observed metastable state is associated with itinerant or localized holes, we simulate  $S(q, \omega)$  for  $p = 0.0938/\text{Cu}_L$  with a local charge impurity (see Fig. 5d). To do this, we impose an additional chemical potential shift  $\Delta\mu = 5t$  that is strong enough to localize the doped holes. We apply the localization potential at site  $(l = l_1, j = j_1)$  near the reference point  $(l = 0, j = j_0)$ , using the same convention as in Eq. (10). The modified Hamiltonian is written as

$$\mathcal{H}'(l_1, j_1) = \mathcal{H} + \Delta\mu \left[ n_{j_1\uparrow}^{(l_1)} + n_{j_1\downarrow}^{(l_1)} \right]. \quad (11)$$

We consider three inequivalent impurity locations: at sites  $(1, j_0)$  (type 1),  $(0, j_0 \pm 1)$  (type 2), and  $(1, j_0 \pm 1)$  (type 3), as shown schematically in Fig. S20. The experimental  $S(q, \omega)$  in the metastable state shows a suppression centered at the two triplon peak, spanning the continuum, and without changing the shape of the dispersion (see Fig. 5d of the main text). The simulated  $S(q, \omega)$  with hole localization deviates from this for all three impurity types. For impurity type 1, spectral weight is significantly suppressed at  $L = 0.25$  and transferred to lower momenta within the two triplon continuum. Impurity type 2 shows an even stronger suppression of the two triplon spectral weight, by almost a factor of two, transferred into the quasiparticle branch at lower energy loss. Impurity type 3 results in a similar redshift of spectral weight as type 2, albeit with a lower magnitude. In all cases, the suppression of the two-triplon continuum is much larger than observed in the experimental  $S(q, \omega)$ . Finally, to reflect the statistical average of randomly distributed

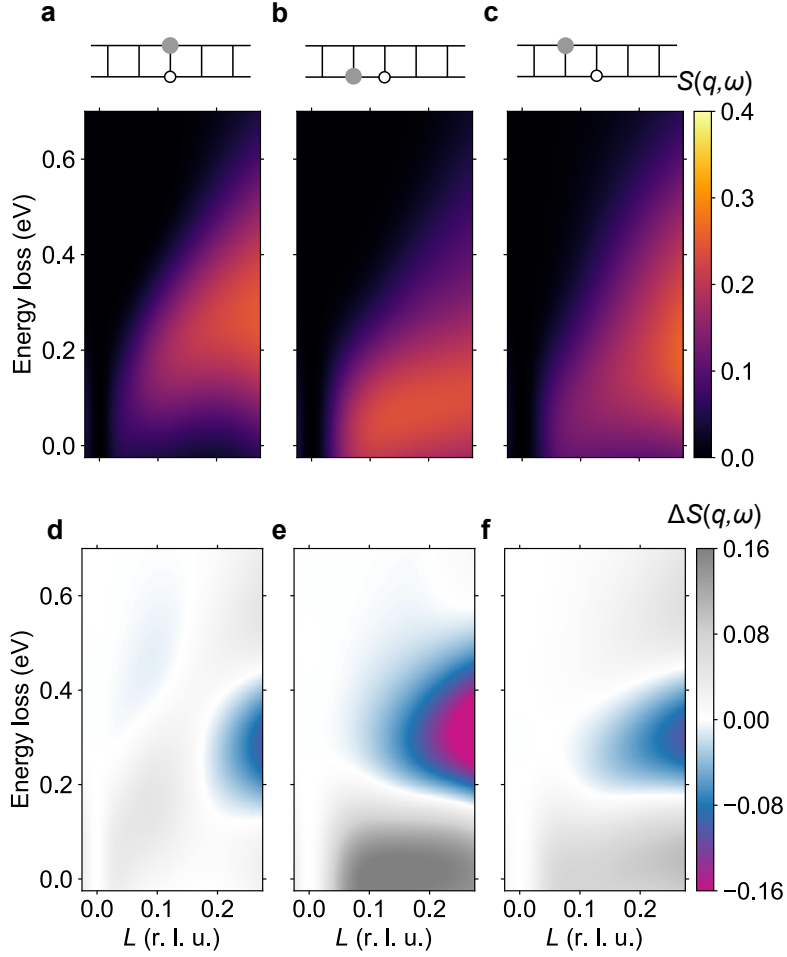


**Fig. S20. Spectral analysis for different localized hole configurations.** **a-c** The  $S(q, \omega)$  calculated for hole density  $p = 0.0938/C_{\text{uL}}$  for three different impurity configurations. The upper schematics illustrate the position of the impurity site (gray dot,  $(l_1, j_1)$ ) relative to the reference site (white dot,  $(0, j_0)$ ) for each of the three impurity configurations. **d-f** Differential intensities  $\Delta S(q, \omega)$  compared to the  $S(q, \omega)$  of the reference state with  $p = 0.0625/C_{\text{uL}}$  (shown in Fig. S17a) for each of the three impurity configurations.

impurities, we calculate a weighted average of these data based on the symmetry and equivalence of the sites. This weighted average, presented in Fig. 5d of the main text, similarly deviates from the experimental observations. Therefore our experimental results are consistent with holes transferred into the ladder, with primarily itinerant character.

## 7. Light-driven symmetry breaking and hopping

The primary mode of interaction between the chains and ladders is via the apical oxygen atoms in the chain [9, 22], as outlined in the main text. The low-energy electronic state of the ladder holes is a Zhang-Rice singlet (ZRS), composed of Cu  $3d_{x^2-y^2}$  and surrounding O  $2p_{x/y}$  orbitals on each plaquette, possessing approximate  $D_{4h}$  symmetry. Owing to its  $d$ -wave character, the ZRS wavefunction switches sign under a  $\pi/2$  rotation around the copper-apical oxygen axis, whereas the O  $2p_z$  orbital remains invariant. As a result, the hopping integral  $t_{\text{ap}}$  between the ZRS and the apical oxygen, which arises from a superposition of four terms involving rotated ZRS configurations with alternating signs, cancels out. Dressing by intense in-plane electric fields breaks this symmetry by introducing an additional Peierls phase to the hopping matrix elements. This perturbation imbalances the superposition of hopping terms involving orbitals aligned with and perpendicular to the electric field, allowing for a finite  $t_{\text{ap}}$  between the ladder and chain. We present a detailed derivation of this result below.

### Simplified theoretical model

The large number of atoms in the unit cell of  $\text{Sr}_{14}\text{Cu}_{24}\text{O}_{41}$  and the strongly correlated nature of this compound render an exact many-body calculation of the full unit cell intractable. This motivates us to identify a suitably simplified model that captures the essential features of the ladders and their weak coupling to the chains.

First, prior diffraction studies [9, 22] show that the shortest ladder-chain bonds are between the subset of Cu and O atoms that are approximately aligned with each other along the apical direction, as shown in Fig. S21. Since hopping drops rapidly with distance, it is reasonable to approximate the chain-ladder hopping in terms of this shortest bond. Second, the Sr  $5s$  energy levels are predominantly located far from the Fermi level as shown by prior LDA calculations [23] as well as our calculations (Fig. S21c), and hence do not contribute significantly to the apical hopping. Finally, the ladder holes form Zhang-Rice singlet states, composed of Cu  $3d_{x^2-y^2}$  and surrounding O  $2p_x/p_y$  orbitals on each plaquette. Based on these features, we construct a  $\text{CuO}_6$  cluster consisting of a  $\text{CuO}_4$  plaquette (representing the ladder) and an apical O atom on

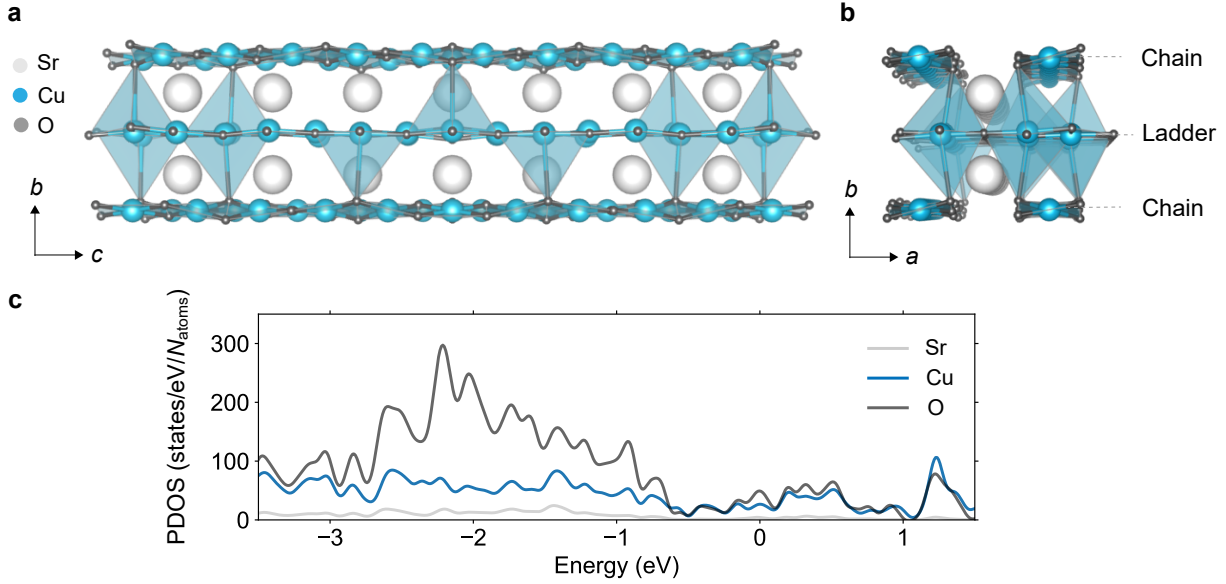


**Fig. S21. Weak Cu-O apical bonds.** **a-b**, The crystal structure of  $\text{Sr}_{14}\text{Cu}_{24}\text{O}_{41}$ . Polyhedra are drawn for all the Cu-O bonds that are shorter than 3 Å. The chain and ladder features are incommensurate with one another, but every few plaquettes along the  $c$  direction, a Cu atom lines up with an approximately apical O. These bond lengths vary from 2.9-3 Å. **c**, The projected density of states (PDOS) for Sr, Cu, and O atoms. The Sr atoms have a negligible contribution to the density of states near the Fermi level.  $N_{\text{atoms}} = 316$  in the supercell.

each side (representing the adjacent chains) as a minimal model for our analytical and *ab initio* quantum chemistry calculations, in order to qualitatively confirm the above theoretical derivations. We position apical atoms on either side of the plaquette to ensure that the cluster maintains inversion symmetry.

### ***d*-wave symmetry of hole carriers and parity mismatch**

We first examine the vertical hopping between the in-plane copper  $3d_{x^2-y^2}$  orbital and the approximately apical oxygen  $2p_z^*$  orbital (\* here indicates the apical oxygen) above it. At the *ab initio* level, this hopping integral is calculated as

$$t_{dpz} = \iiint \psi_{2p_z}^*(\mathbf{r}) \mathcal{H} \psi_{3d_{x^2-y^2}}(\mathbf{r}) d\mathbf{r}^3, \quad (12)$$

where  $\psi_{2p_z}(\mathbf{r})$  and  $\psi_{3d_{x^2-y^2}}(\mathbf{r})$  are the Wannier wavefunctions of the apical oxygen  $2p_z^*$  and in-plane copper  $3d_{x^2-y^2}$  orbitals, respectively. Here,  $\mathcal{H}$  is the electronic Hamiltonian and can be regarded as the single-electron part of the many-body Hamiltonian for the purpose of evaluating the hopping integral. While single-electron

integrals are usually evaluated numerically in quantum chemistry, symmetry analysis can determine whether the integral will vanish or not. Since the centers of these wavefunctions are approximately aligned along the copper-apical oxygen line, we define a rotational operator  $\hat{R}(\theta)$  about this axis. The  $3d_{x^2-y^2}$  and  $2p_z$  orbitals exhibit different parities under  $\pi/2$  rotations

$$\hat{R}\left(\frac{\pi}{2}\right)\psi_{2p_z}(\mathbf{r}) = \psi_{2p_z}(\mathbf{r}), \quad \text{and} \quad \hat{R}\left(\frac{\pi}{2}\right)\psi_{3d_{x^2-y^2}}(\mathbf{r}) = -\psi_{3d_{x^2-y^2}}(\mathbf{r}). \quad (13)$$

If we assume a perfect  $D_{4h}$  symmetry, the Hamiltonian will be symmetric under these rotations, namely  $\hat{R}\left(\frac{\pi}{2}\right)\mathcal{H} = \mathcal{H}$ . Under such symmetry, we can then split the hopping integral as shown below.

$$\begin{aligned} t_{dpz} &= \frac{1}{4} \left[ \iiint \psi_{2p_z}^*(\mathbf{r}) \mathcal{H} \psi_{3d_{x^2-y^2}}(\mathbf{r}) d\mathbf{r}^3 + \hat{R}\left(\frac{\pi}{2}\right) \iiint \psi_{2p_z}^*(\mathbf{r}) \mathcal{H} \psi_{3d_{x^2-y^2}}(\mathbf{r}) d\mathbf{r}^3 \right. \\ &\quad \left. + \hat{R}(\pi) \iiint \psi_{2p_z}^*(\mathbf{r}) \mathcal{H} \psi_{3d_{x^2-y^2}}(\mathbf{r}) d\mathbf{r}^3 + \hat{R}\left(\frac{3\pi}{2}\right) \iiint \psi_{2p_z}^*(\mathbf{r}) \mathcal{H} \psi_{3d_{x^2-y^2}}(\mathbf{r}) d\mathbf{r}^3 \right] \\ &= \frac{1}{4} \left[ \iiint \psi_{2p_z}^*(\mathbf{r}) \mathcal{H} \psi_{3d_{x^2-y^2}}(\mathbf{r}) d\mathbf{r}^3 - \iiint \psi_{2p_z}^*(\mathbf{r}) \mathcal{H} \psi_{3d_{x^2-y^2}}(\mathbf{r}) d\mathbf{r}^3 \right. \\ &\quad \left. + \iiint \psi_{2p_z}^*(\mathbf{r}) \mathcal{H} \psi_{3d_{x^2-y^2}}(\mathbf{r}) d\mathbf{r}^3 - \iiint \psi_{2p_z}^*(\mathbf{r}) \mathcal{H} \psi_{3d_{x^2-y^2}}(\mathbf{r}) d\mathbf{r}^3 \right] \\ &= 0. \end{aligned} \quad (14)$$

Owing to the perfect cancellation of the four possible hopping integrals, the apical oxygen  $2p_z^*$  orbital and the in-plane copper  $3d_{x^2-y^2}$  orbital are completely decoupled from each other.

While our ladder system does not perfectly satisfy the  $D_{4h}$  symmetry due to half-lattice shifts between neighboring ladders, the four oxygen atoms surrounding each copper atom still form an approximately square plaquette, with the Cu-O bond length varying within the range 1.96 - 2.00 Å along the leg direction and 1.92 - 1.97 Å along the rung direction. Moreover, the single-electron integrals between the valence orbitals of adjacent ladders are zero due to the parity mismatch between the orbitals, which effectively suppresses interladder coupling. Consequently, although the hopping  $t_{dpz}$  is not exactly zero in  $\text{Sr}_{14-x}\text{Ca}_x\text{Cu}_{24}\text{O}_{41}$ , it is small compared to that induced by the laser (discussed further in the next subsection).

Since cuprates are charge transfer compounds, with the in-plane Cu-O states exhibiting covalent character, low-energy electronic states due to hole doping are distributed across the Cu and in-plane O atoms [24, 25]. This implies that we also need to consider hopping involving O  $2p$  orbitals along the  $x$  (leg) and  $y$  (rung) directions. Unlike the central Cu  $3d$  orbitals, these O orbitals are not aligned with the apical oxygen, and exhibit finite hopping integrals denoted as  $t_{pp}$ . Our single-unit-cell *ab initio* calculation indicates a hopping  $t_{pp} \sim 0.27$  eV, consistent with the value in high- $T_C$  cuprates such as  $\text{La}_{2-x}\text{Ba}_x\text{CuO}_4$  [26, 27]. Hence, in self-doped  $\text{Sr}_{14-x}\text{Ca}_x\text{Cu}_{24}\text{O}_{41}$  ladders, in-plane and apical oxygens can, in principle, allow chain-to-ladder hopping.

However, doped carriers in the O orbitals form Zhang-Rice singlets that obey the same symmetry as the central  $3d_{x^2-y^2}$  orbital [28]. The other bonding and antibonding states are at higher energies and remain unoccupied [29]. To estimate the effective hopping between the Zhang-Rice singlet and the apical oxygen, we define an effective oxygen wavefunction on each copper site as a symmetric superposition

$$\psi_p(\mathbf{r}; \mathbf{R}) = \frac{1}{2} \left[ \psi_{p_x}(\mathbf{r}; \mathbf{R} - \frac{a_0}{2} \hat{x}) - \psi_{p_x}(\mathbf{r}; \mathbf{R} - \frac{a_0}{2} \hat{x}) + \psi_{p_y}(\mathbf{r}; \mathbf{R} - \frac{a_0}{2} \hat{y}) - \psi_{p_y}(\mathbf{r}; \mathbf{R} + \frac{a_0}{2} \hat{y}) \right]. \quad (15)$$

This effective wavefunction is antisymmetric under rotations of  $\pi/2$ , as

$$\hat{R} \left( \frac{\pi}{2} \right) \psi_p(\mathbf{r}; \mathbf{R}) = -\psi_p(\mathbf{r}; \mathbf{R}), \quad (16)$$

which is the same symmetry observed in the copper  $3d_{x^2-y^2}$  orbital. As a consequence, the hopping between the in-ladder oxygen  $p_{x/y}$  orbital and the apical oxygen  $p_z^*$  orbital also vanishes:

$$\begin{aligned} t_{ppz} &= \frac{1}{4} \left[ \iiint \psi_{2p_z}^*(\mathbf{r}) \mathcal{H} \psi_p(\mathbf{r}) d\mathbf{r}^3 - \iiint \psi_{2p_z}^*(\mathbf{r}) \mathcal{H} \psi_p(\mathbf{r}) d\mathbf{r}^3 \right. \\ &\quad \left. + \iiint \psi_{2p_z}^*(\mathbf{r}) \mathcal{H} \psi_p(\mathbf{r}) d\mathbf{r}^3 - \iiint \psi_{2p_z}^*(\mathbf{r}) \mathcal{H} \psi_p(\mathbf{r}) d\mathbf{r}^3 \right] \\ &= 0. \end{aligned} \quad (17)$$

Since both  $t_{dpz}$  and  $t_{pp}$  vanish, the vertical charge transfer between the ladder and the apical oxygen also vanishes.

## Chain-ladder hopping triggered by laser field

The  $D_{4h}$  symmetry may be broken by the pump electric field, leading to a light-induced charge transfer between chains and ladders. While the symmetry of the Hamiltonian is preserved when we apply an out-of-plane polarized ( $E \parallel b$ ) pump to the system, the  $C_4$  symmetry of the  $\text{CuO}_4$  plaquette can be broken by an in-plane polarized ( $E \parallel a$  or  $E \parallel c$ ) electric field. We linearize the field dependence of the Hamiltonian as

$$\mathcal{H}(\mathbf{A}) = \mathcal{H}(\mathbf{A} = 0) - \frac{e}{2m_e c} \sum_j [i\hbar \nabla_j \cdot \mathbf{A}(\mathbf{r}_j) + h.c.] + O(\mathbf{A}^2), \quad (18)$$

and, choosing the polarization as  $\mathbf{A}(\mathbf{r}_j) = A_0(\mathbf{r})\hat{x}$ , we rewrite the hopping as

$$t_{ppz} = \iiint \psi_{2p_z}^*(\mathbf{r}) \left[ \mathcal{H}(A_0 = 0) - \frac{i\hbar e}{m_e c} [A_0(\mathbf{r}) \frac{\partial}{\partial x} + \frac{\partial A_0(\mathbf{r})}{\partial x}] + O(A_0^2) \right] \psi_p(\mathbf{r}) d\mathbf{r}^3. \quad (19)$$

As discussed in the prior section, the first equilibrium term vanishes. Since the linear term exhibits odd parity, and both  $\psi_{2p_z}$  and  $\psi_p$  have even parity, this term will also vanish, implying that the hopping in the presence of an optical pump is proportional to the square of the field strength. This conclusion also applies to  $t_{dpz}$ , the hopping integral between the Cu  $3d_{x^2-y^2}$  orbital and the apical O  $2p_z$  orbital.

The second-order field dependence for the oxygen orbitals can be evaluated by using the Peierls substitution due to the separation of charge centers. The effect of the external vector potential is simplified into a location-dependent phase factor in the hopping integral. For two Bloch wavefunctions centered at sites  $\mathbf{r}_i$  and  $\mathbf{r}_j$ , the hopping integral becomes

$$t(\mathbf{r}_i, \mathbf{r}_j) \rightarrow t(\mathbf{r}_i, \mathbf{r}_j) \exp\left(\frac{ie}{\hbar c} \int_{\mathbf{r}_i}^{\mathbf{r}_j} \mathbf{A}(\mathbf{r}) \cdot d\mathbf{r}\right). \quad (20)$$

Thus, we estimate the light-driven hopping integral between the bonding oxygen wavefunctions in the ladder and the  $2p_z$  orbital of the apical oxygen in the chain as

$$t_{ppz} = \frac{1}{2} (t_{pp} + t_{pp} - t_{pp} e^{-i\frac{eA_0 a_0}{2\hbar c}} - t_{pp} e^{i\frac{eA_0 a_0}{2\hbar c}}) = t_{pp} \left[ 1 - \cos\left(\frac{eA_0 a_0}{2\hbar c}\right) \right] \simeq \frac{1}{2} \left(\frac{eA_0 a_0}{2\hbar c}\right)^2 t_{pp} \propto A_0^2. \quad (21)$$

This result shows that the  $t_{ppz}$  matrix element, which vanishes at equilibrium, becomes nonzero due to the applied electric field, and its amplitude scales linearly with the field intensity. Our *ab initio* simulation using a  $\text{CuO}_6^{9-}$  cluster, that is a  $\text{CuO}_6^{10-}$  ionic compound with a doped hole, confirms this square scaling with the electric field, giving  $t_{ppz} \approx 1.08 \text{ meV}$  for  $E = 7 \text{ MV/cm}$ .

One may further consider the steady-state renormalization of the hopping matrix elements in the presence of the optical pump. The effective period-averaged hopping integral can be expressed as

$$t_{ppz}^{(\text{eff})} = \frac{2\pi}{\Omega} \int_0^{2\pi/\Omega} t_{pp} \left[ 1 - \cos \left( \frac{ea_0 A_0 \cos(\Omega\tau)}{2\hbar c} \right) \right] d\tau = \left[ 1 - \mathcal{J}_0 \left( \frac{ea_0 A_0}{2\hbar c} \right) \right] t_{pp}. \quad (22)$$

Here,  $\mathcal{J}_0(z)$  is the Bessel function of the first kind. In the weak-pump limit, the hopping integral is also proportional to  $A_0^2$  at the leading order. Incorporating this value into the *ab initio* simulation, we obtain  $t_{ppz}^{(\text{eff})} \approx 0.54 \text{ meV}$  for  $E = 7 \text{ MV/cm}$ .

## Pump-induced energy shift of ladder and chain orbitals

The optically activated hopping described in the previous section determines the rate of the hole transfer and establishes metastability. On the other hand, the direction of hole transfer as well as the overall number of transferred holes is determined by the difference in the optically-dressed orbital energies, as we outline below.

Similar to the one-electron integral Eq. (19), the energy of any of the relevant orbitals in the presence of the vector potential is given by

$$\epsilon_\alpha(\mathbf{A}) = \iiint \psi_\alpha(\mathbf{r}) \left[ \hat{H}(\mathbf{A} = 0) - i \frac{e\hbar}{2m_e c} \frac{\partial A_0(\mathbf{r})}{\partial x} - i A_0(\mathbf{r}) \frac{e\hbar}{m_e c} \frac{\partial}{\partial x} + O(\mathbf{A}^2) \right] \psi_\alpha(\mathbf{r}) d\mathbf{r}^3, \quad (23)$$

where  $\alpha = 3d_{x^2-y^2}, 2p_x, 2p_y,$  or  $2p_z^*$ . The first term of the integral gives the equilibrium orbital energy, denoted as  $\epsilon_\alpha^{(\text{eq})}$ . Since all relevant orbital wavefunctions are either even or odd under inversion, their squares (density) are always even, leading to the vanishing of the second and third terms. Therefore, all orbital energies, and hence the total hole transfer in the metastable state, are expected to change quadratically with the external field  $\mathbf{A}$ , or equivalently, the electric field strength  $\mathbf{E} = -\partial\mathbf{A}/\partial t$ .

We verify this quadratic dependence by simulating the Hartree-Fock orbital energy of a  $\text{CuO}_6^{9-}$  cluster. The Zhang-Rice singlet states in the ladder (consisting of the covalently bonded Cu  $3d_{x^2-y^2}$  and O  $2p_x/p_y$  orbitals) are spatially extended, with a quadrupole comparable to the square of the lattice constant. On the other hand, the apical O  $p_z$  orbital in the chain has a negligible quadrupole. Due to this geometric distinction, the in-plane pump results in a substantial energy increase for electrons in the ladder, and a negligible impact on those in the chain. The energy imbalance results in a net transfer of holes from the chain to the ladder. As shown in Fig. S22a, the energy difference between the Cu  $3d_{x^2-y^2}$  and apical oxygen  $2p_z$  orbitals increases linearly with  $|\mathbf{E}|^2$ , as does the difference between the in-plane and apical oxygen orbitals. We further validate this conclusion by simulating the partial charge of the apical oxygens in the  $\text{CuO}_6^{9-}$  cluster with a correlation-consistent basis (here, we used the cc-pVTZ basis). While these single-unit-cell simulations cannot model itinerant behavior, which is necessary for a quantitative description of the observed charge transfer, they can reliably capture qualitative trends. The light-induced electron density increases quadratically with the pump field, as shown in Fig. 22b. This is consistent with the experimental pump field dependence of the differential ladder and chain XAS intensities in the metastable state.

To provide an order-of-magnitude estimation of the total charge transfer in the experimental system with itinerant electrons, we evaluate the compressibility of the ladder system by ignoring interactions. We find that the total light-induced energy shift obtained from our ab initio calculations results in a 2% charge transfer, consistent with the experimentally observed 3% light-induced doping, further corroborating the mechanism of hole transfer and metastability.

### Hole transfer due to deviations from the $D_{4h}$ symmetry

Our theoretical picture assumes perfect  $D_{4h}$  symmetry at equilibrium for simplicity. However, the quasi-1D crystal structure of  $\text{Sr}_{14-x}\text{Ca}_x\text{Cu}_{24}\text{O}_{41}$  slightly breaks this symmetry at equilibrium. Specifically, the Cu-O bond length along the leg direction is slightly larger than that on the rung. To estimate the impact of this asymmetry, we calculate the charge transfer resulting from a breaking of the  $D_{4h}$  symmetry at equilibrium. We take the average bond length to be  $\sim 1.98 \text{ \AA}$  along the leg direction and  $\sim 1.945 \text{ \AA}$  along the rungs.

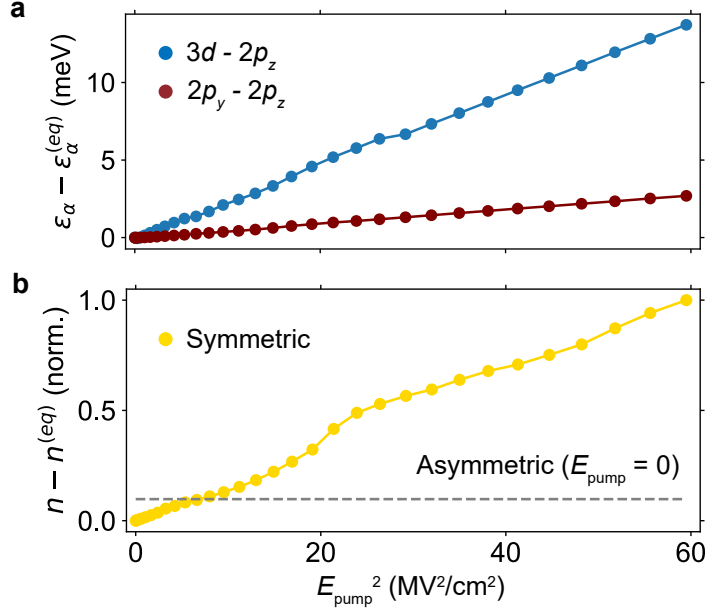


**Fig. S22. Quadratic dependence of site energy and charge density with the external field.** **a**, Energy difference between  $3d_{x^2-y^2}$  and  $2p_z$  orbitals (blue), and between  $2p_y$  and  $2p_z$  orbitals (maroon) as function of the squared electric field for a  $\text{CuO}_6^{9-}$  cluster with a symmetrical plaquette (Cu-O bond length =  $1.96\text{\AA}$ ). **b**, Normalized charge density change on the apical O atom as function of the squared electric field. The grey dashed line denotes the normalized charge density for an unpumped asymmetric plaquette with Cu-O bond length of  $1.945\text{\AA}$  along the rung and  $1.98\text{\AA}$  along the leg.

Since the geometric asymmetry may lead to different configurations of molecular orbitals, we do not compare the orbital energy and instead directly focus on its effect on the chain-to-ladder hole transfer. As shown in Fig. 22b, this slight geometric asymmetry contributes an initial charge transfer that is an order of magnitude smaller than that due to the pump field. Therefore, we neglect equilibrium deviations from the  $D_{4h}$  symmetry in the discussion of our results.

## References

- [1] Thorsmølle, V. *et al.* Phonon Energy Gaps in the Charged Incommensurate Planes of the Spin-Ladder  $\text{Sr}_{14}\text{Cu}_{24}\text{O}_{41}$  Compound by Raman and Infrared Spectroscopy. *Physical Review Letters* **108**, 217401 (2012).
- [2] Vuletić, T. *et al.* Suppression of the Charge-Density-Wave State in  $\text{Sr}_{14}\text{Cu}_{24}\text{O}_{41}$  by Calcium Doping. *Physical Review Letters* **90**, 257002 (2003).
- [3] Abbamonte, P. *et al.* Crystallization of charge holes in the spin ladder of  $\text{Sr}_{14}\text{Cu}_{24}\text{O}_{41}$ . *Nature* **431**, 1078–1081 (2004).
- [4] Nücker, N. *et al.* Hole distribution in  $(\text{Sr,Ca,Y,La})_{14}\text{Cu}_{24}\text{O}_{41}$  ladder compounds studied by x-ray absorption spectroscopy. *Physical Review B* **62**, 14384 (2000).
- [5] Huang, M.-J. *et al.* Determination of hole distribution in  $\text{Sr}_{14-x}\text{Ca}_x\text{Cu}_{24}\text{O}_{41}$  using soft x-ray absorption spectroscopy at the Cu  $L_3$  edge. *Physical Review B* **88**, 014520 (2013).
- [6] Osafune, T., Motoyama, N., Eisaki, H. & Uchida, S. Optical Study of the  $\text{Sr}_{14-x}\text{Ca}_x\text{Cu}_{24}\text{O}_{41}$  System: Evidence for Hole-Doped  $\text{Cu}_2\text{O}_3$  Ladders. *Physical Review Letters* **78**, 1980 (1997).
- [7] Tseng, Y. *et al.* Crossover of high-energy spin fluctuations from collective triplons to localized magnetic excitations in  $\text{Sr}_{14-x}\text{Ca}_x\text{Cu}_{24}\text{O}_{41}$  ladders. *npj Quantum Materials* **7**, 92 (2022).
- [8] Chen, C. *et al.* Electronic states in  $\text{La}_{2-x}\text{Sr}_x\text{CuO}_{4+\delta}$  probed by soft-x-ray absorption. *Physical Review Letters* **66**, 104 (1991).
- [9] Deng, G. *et al.* Structural evolution of one-dimensional spin-ladder compounds  $\text{Sr}_{14-x}\text{Ca}_x\text{Cu}_{24}\text{O}_{41}$  with Ca doping and related evidence of hole redistribution. *Physical Review B* **84**, 144111 (2011).
- [10] Wang, Y., Fabbri, G., Dean, M. P. M. & Kotliar, G. EDRIXS: An open source toolkit for simulating spectra of resonant inelastic x-ray scattering. *Computer Physics Communications* **243**, 151–165 (2019).
- [11] Ament, L. J., Ghiringhelli, G., Sala, M. M., Braicovich, L. & van den Brink, J. Theoretical demonstration of how the dispersion of magnetic excitations in cuprate compounds can be determined using resonant inelastic X-ray scattering. *Physical Review Letters* **103**, 117003 (2009).
- [12] Robarts, H. C. *et al.* Dynamical spin susceptibility in  $\text{La}_2\text{CuO}_4$  studied by resonant inelastic x-ray scattering. *Physical Review B* **103**, 224427 (2021).
- [13] Jia, C. *et al.* Persistent spin excitations in doped antiferromagnets revealed by resonant inelastic light scattering. *Nature Communications* **5**, 3314 (2014).
- [14] Shen, Y. *et al.* Role of oxygen states in the low valence nickelate  $\text{La}_4\text{Ni}_3\text{O}_8$ . *Physical Review X* **12**, 011055 (2022).
- [15] Padma, H. *et al.* (forthcoming) (2024).
- [16] Chen, Z. *et al.* Anomalously strong near-neighbor attraction in doped 1D cuprate chains. *Science* **373**, 1235–1239 (2021).

- [17] Wang, Y. *et al.* Phonon-mediated long-range attractive interaction in one-dimensional cuprates. *Physical Review Letters* **127**, 197003 (2021).
- [18] Troyer, M., Tsunetsugu, H. & Rice, T. Properties of lightly doped  $t$ - $J$  two-leg ladders. *Physical Review B* **53**, 251 (1996).
- [19] Liu, S., Jiang, H.-C. & Devereaux, T. P. Nature of a single doped hole in two-leg Hubbard and  $t$ - $J$  ladders. *Physical Review B* **94**, 155149 (2016).
- [20] Kumar, U., Nocera, A., Dagotto, E. & Johnston, S. Theoretical study of the spin and charge dynamics of two-leg ladders as probed by resonant inelastic x-ray scattering. *Physical Review B* **99**, 205130 (2019).
- [21] Schlappa, J. *et al.* Collective Magnetic Excitations in the Spin Ladder  $\text{Sr}_{14}\text{Cu}_{24}\text{O}_{41}$  Measured Using High-Resolution Resonant Inelastic X-Ray Scattering. *Physical Review Letters* **103**, 047401 (2009).
- [22] Gotoh, Y. *et al.* Structural modulation, hole distribution, and hole-ordered structure of the incommensurate composite crystal  $(\text{Sr}_2\text{Cu}_2\text{O}_3)_{0.70}\text{CuO}_2$ . *Physical Review B* **68**, 224108 (2003).
- [23] Arai, M. & Tsunetsugu, H. Electronic structures of  $\text{Sr}_{14-x}\text{Ca}_x\text{Cu}_{24}\text{O}_{41}$ . *Physical Review B* **56**, R4305 (1997).
- [24] Zaanen, J. & Gunnarsson, O. Charged magnetic domain lines and the magnetism of high-T c oxides. *Physical Review B* **40**, 7391 (1989).
- [25] Imada, M., Fujimori, A. & Tokura, Y. Metal-insulator transitions. *Reviews of Modern Physics* **70**, 1039 (1998).
- [26] McMahan, A., Annett, J. F. & Martin, R. M. Cuprate parameters from numerical Wannier functions. *Physical Review B* **42**, 6268 (1990).
- [27] McMahan, A., Martin, R. M. & Satpathy, S. Calculated effective Hamiltonian for  $\text{La}_2\text{CuO}_4$  and solution in the impurity Anderson approximation. *Physical Review B* **38**, 6650 (1988).
- [28] Zhang, F. & Rice, T. Effective Hamiltonian for the superconducting Cu oxides. *Physical Review B* **37**, 3759 (1988).
- [29] Kung, Y. *et al.* Characterizing the three-orbital Hubbard model with determinant quantum Monte Carlo. *Physical Review B* **93**, 155166 (2016).